A Particle Telescope Verification at an Accelerator Facility

Noriega Benítez, Enriqueta A Particle Telescope Verification at an Accelerator
Facility

The environment around Earth hosts several particle populations. This region is affected by particles from the galactic cosmic rays, solar wind, and the trapped particles in the radiation belts [1]. The solar wind carries energetic electrons, protons, and heavy ions into space. These conditions deeply affect our presence in the near-Earth environment. Protons and heavy ions can damage satellites, they can also trigger radiation hazards at aviation altitudes, and radio communications can experience interference [2]. Energetic charged particles can affect spacecraft electronics. It is vital to analyse satellite anomalies and to understand the particles' path through the magnetosphere. The number of orbiting satellites in the near-Earth environment is growing. The presence of satellites and spacecraft creates much debris that is also on the rise. Eventually, our use of space can be threatened if further studies are not carried out [3]. Earth's magnetic field provides the conditions for the particle populations to inhabit the region. However, the near-Earth radiation environment is deeply affected by the solar wind and the magnetospheric processes.

FORESAIL-1 is a nanosatellite mission that aims to assess the environment in the near-Earth space with sustainable deorbiting technology. The mission will observe energetic particles in the radiation belts, quantify electronic precipitation, and measure energetic neutral atoms of solar origin. Its findings shall improve our understanding of solar eruption energy and can provide in site data of the near-Earth radiation environment. FORESAIL-1 carries PATE, a Finnish particle telescope onboard. [4]

This thesis presents the the method for the instrument calibration and results of a calibration rehearsal for the future analysis of data captured by PATE, during its calibration campaign. PATE has undergone preliminary tests at the RADEF cyclotron facility of the University of Jyväskylä, where it was exposed to monoenergetic proton beams. Using its eight active detector areas, PATE detected particle hits from the 10.5 MeV and 55 MeV proton beams at various angles and energies. Using a Geant4 model, we were able to simulate how the detector would respond to different conditions and predict the number of events within a range of particle energies.The simulations were adapted to controlled conditions that sought to replicate the testing facility RADEF environment. Here, we discuss the similarities and mismatches between the pulse-height data recorded and simulated for the 10.5 MeV beam, highlight possible solutions, and explain what the discrepancies can teach us about the detector and our current understanding of its operation.

Keywords: particle detection, calibration, magnetosphere

Contents

1 Introduction

The Earth's atmosphere, ionosphere, and magnetosphere encompass an observable environment that enables the study of the near Sun environment and its impact on near-Earth space [5]. Many of the particles involved in the near-Earth environment originate from the Sun. The particles released in solar process are mainly electrons and protons, but there is also a small amount of ionised helium and heavy ions. These particles travel through space an interact with Earth magnetic field from an early proximity. This interaction affects the solar wind flow and the behaviour of Earth's magnetic field. Although it is clear that the interactions between the Sun and Earth's magnetosphere and atmosphere are essential, the research in this field is highly topical. New insights are constantly adding to our understanding. The availability of new technology facilitates the collection of more specific data using ground-based technology and satellites. Sustained growth in the topic is leading to new studies of near-Earth space, solar wind and highly energetic cosmic rays.

The space-borne experiments are influenced by the environmental hazards they face during their observations. Space particle detection experiments need to survive the conditions present in the environments in which they are launched, specifically in the radiation belts engulfing Earth. The radiation belts are toroidal regions around the Earth where the geomagnetic field traps particles and confines them. The radiation belts are highly dynamic and host multiple processes through which particles interact with each other and diffuse. An accepted explanation for why radiation belts diffuse and how particles are preserved after they were trapped is given by the adiabatic theory of charged-particle motion. However, the exact explanation is yet to be understood. There are some questions to be answered and there are different attempts trying to understand the different processes we observe, for instance, an exact explanation for the dynamical processes that dictate the injection and loss of radiation-belt particle populations. [6]

The near-Earth space hosts multiple energetic processes resulting in charged particles being injected into the radiation belts, accelerated, and eventually lost in the upper atmosphere that are commonly called the space weather [7]. The space weather is a collection of phenomena between the Sun and Earth; in a manner analogous to meteorological weather, space weather can present similar conditions set in the space environment. Radiation belts are a key player in near-Earth space weather. The environment they provide can affect spacecraft and its subsystems. The electron fluxes change over time variations as a function of distance and energy, abiding by magnetospheric processes [8]. The outer radiation belt suffers losses through the outer edge of the magnetosphere, through the radially outward displacement of electrons carried by waves, and through wave-particle interactions that scatter particles into the upper atmosphere. This precipitation of particles is absorbed by the gaseous atmosphere. [9]

Observations, simulations, and theory provide a wide panorama that can improve our understanding of physical processes and their impact on the near-Earth space environment. The particles observed along their trajectory towards Earth and its nearby environment are mainly electrons, protons, and heavier nuclei [10]. They can be accelerated from solar flares and coronal mass ejection (CME)-driven, interplanetary (IP) shocks [9]. The particles around Earth and in IP space are known as solar energetic particles (SEPs). There are different particle populations: impulsive SEP events are accelerated by flares, gradual SEP events are originated through near-Sun CME-shocks, and energetic storm particle (ESP) events are produced during CME shocks [6].

Particle Telescope (PATE) is a miniature instrument designed to make particle observations in the near-Earth environment. PATE's mission seeks to quantify the loss of electrons from the outer belt by precipitation in the atmosphere. Another scientific objective is to measure the energetic neutral atoms that result from charge-

exchange processes in the solar corona.

2 Theoretical background

2.1 Particle Dynamics

Charged particle motion can be described by the equation

$$\frac{d\mathbf{p}}{dt} = q(\mathbf{E} + \mathbf{v} \times \mathbf{B}) + \mathbf{F}_{\text{ext}}, \tag{1}$$

where $\mathbf{p}$ is the momentum, q is the particle's charge, $\mathbf{E}$ is the electric field, $\mathbf{v}$ is the particles velocity, $\mathbf{B}$ is the magnetic field, and $\mathbf{F}_{\text{ext}}$ includes the external forces acting on the particle that are not electromagnetic forces. $\mathbf{F}_{\text{ext}}$ commonly only describes the gravitational force, which is often negligible compared to the electromagnetic forces present. Equation (1) is called the Newton-Lorentz force equation and it can be solved under different approximations. [11]

2.1.1 Gyration

Let us consider a non-relativistic charged particle in a constant uniform magnetic field $\mathbf{B}$ in the absence of an electric field. From equation (1) we have

$$m\frac{d\mathbf{v}}{dt} = q(\mathbf{v} \times \mathbf{B}),$$

where m is the particle's mass and $m\mathbf{v} = \mathbf{p}$. Let us align the magnetic field $\mathbf{B}$ along the z-axis, then $\mathbf{B} = B\hat{k}$ and the components are described as,

$$m\dot{v}_x = qBv_y$$
$$m\dot{v}_y = -qBv_x$$
$$m\dot{v}_z = 0 \implies v_z = \text{const},$$

where a dot represents a time derivative. The second derivatives of the velocity components are

$$\implies \ddot{v}_x = \frac{qB}{m} \cdot \dot{v}_y$$

$$\ddot{v}_y = -\frac{qB}{m} \cdot \dot{v}_x$$

$$\implies \ddot{v}_x = \frac{qB}{m} \cdot -\frac{qB}{m} v_x$$

$$\ddot{v}_y = -\frac{qB}{m} \cdot \frac{qB}{m} v_y,$$

Setting $\omega_c = qB/m$ gives

$$\implies \ddot{v}_x = -\omega_c{}^2 v_x$$

$$\ddot{v}_y = -\omega_c{}^2 v_y,$$

which describe a harmonic oscillator with an angular frequency ω_c. The magnetic field does not affect the particle's kinetic energy and it is conserved through the motion as $\frac{m\mathbf{v^2}}{2} = \text{const} \implies \mathbf{v^2} = v_x{}^2 + v_y{}^2 + v_z{}^2 = \text{const} \implies v_x{}^2 + v_y{}^2 = \text{const}$ since v_z does not change. This equation describes a circular movement in the XY-plane. The radius can be determined by

$$r_L = \frac{mv_\perp}{|q|B}, \tag{2}$$

where $v_\perp = \sqrt{v_x{}^2 + v_y{}^2}$. r_L is also known as the Larmor radius. The *guiding centre* of *gyration* is the central point of the circular movement. The rotation period around it takes time τ_L:

$$\tau_L = \frac{2\pi m}{|qB|}, \tag{3}$$
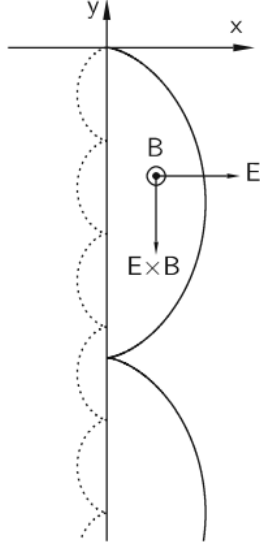
where τ_L is the Larmor period. [11]

Figure 1. Motion of ions (full line) and electrons (dashed line) in a cycloid trajectory in the presence of gyro-motion and $\mathbf{E}\times\mathbf{B}$-drift. Here $\mathbf{E}$ is along the X-axis and $\mathbf{B}$ is perpendicular to the XY-plane. Image credit: [11].

2.1.2 Drift

Let $\mathbf{E}$ be constant. Then from (1) the equation for the parallel-to-$\mathbf{E}$ component of the velocity is

$$m\dot{v}_\parallel = qE_\parallel$$

Consider the perpendicular electric field along the X-axis, then,

$$\dot{v}_x = \omega_c v_y + \frac{q}{m}E_x \qquad\qquad \Rightarrow \ddot{v}_x = -\omega_c^2 v_x$$

$$\dot{v}_y = -\omega_c v_x \qquad\qquad \ddot{v}_y = -\omega_c^2\left(v_y + \frac{E_x}{B}\right)$$

This is harmonic oscillation in the X-direction but the motion in Y-direction is more complex. In a frame of reference moving at constant velocity, $-E_x/B$ in the negative y-axis direction, $v'_y = v_y + E_x/B$. The *electrical drift velocity* $\mathbf{v}_E$ is

$$\mathbf{v}_E = \frac{\mathbf{E}\times\mathbf{B}}{B^2} \tag{4}$$

this last expression is independent of charge and mass. An electric drift motion is shown in Figure 1. A more general form of (4) to describe the drift is

$$\mathbf{v}_D = \frac{\mathbf{F}_\perp \times \mathbf{B}}{qB^2} \tag{5}$$

where $\mathbf{F}_\perp$ is $\mathbf{F} = q\mathbf{E}$ the force acting on the particles.

2.1.3 Bounce

The circular movement of the charged particle along field lines can induce and electric ring current I with its own magnetic momentum μ pointing at the opposite direction of $\mathbf{B}$. The particle's motion describes a circle of radius r_L and area A in a time period of τ_L. Then the magnetic moment is

$$|\mu| = IA = \frac{|q|}{\tau_L}\pi r_L{}^2 = |q|\frac{\omega_c}{2\pi}\pi\left(\frac{v_\perp}{\omega_c}\right)^2 = m\frac{mv_\perp{}^2}{2B} = \frac{W_\perp}{B} \tag{6}$$

After going round it circular trajectory the particle gains additional energy known as energy of perpendicular motion, $W_\perp$, analogously there is a parallel motion $W_\parallel$. The total energy is W and the magnetic moment is $\mu = W_\perp/B$ which are conserved in the gyration approximation in section (2.1.1). This means that when a particle moves towards a growing B, $W_\perp$ grows while $W_\parallel$ decreases. The pitch angle (α) of a particle in a magnetic field is the angle between the magnetic field and the particle momentum. The magnetic moment can also be in terms of the pitch angle, in this case $v_\perp = v\sin\alpha$ and thus,

$$\mu = \frac{mv^2\sin^2\alpha}{2B}.$$

In this expression only α and B are variables when the magnetic momentum is conserved. Then at any two points with $B1$ and $B2$, and α_1 and α_2 respectively,

$$\frac{\sin^2\alpha_1}{\sin^2\alpha_2} = \frac{B_1}{B_2}$$

The particle is experiencing an additional force antiparallel to **B** from the Lorentz force term in (1). This force is known as *mirror force*, $\mathbf{F} = -\mu\nabla_\parallel B$ and it "reflects" the motion of the particle back. When the pitch angle is greater than 90°, mirroring occurs; if it is less, then it escapes.

A *magnetic bottle* is created when the magnetic field lines form two magnetic mirrors at their ends. The pitch angle has to be between

$$\arcsin\sqrt{\frac{B_0}{B_m}} \leq \alpha_0 \leq 180° - \arcsin\sqrt{\frac{B_0}{B_m}}$$

for the particle to be trapped. Here B_m is the mirror magnetic field magnitude at the mirroring points, and B_0 is the reference field magnitude set at the equator at equal distance from the mirroring points. If the particle has a pitch angle outside the range it escapes the magnetic bottle, in this case the particle resides in the *loss cone.* The loss cone is the group of angles at which a particle will be able to penetrate the magnetic bottle deep enough to end up in the upper atmosphere and no longer be trapped in the magnetosphere. [11]

Particles trapped in the magnetic bottle have periodic-like motion. The bounce period is

$$\tau_b = 2\int_{s_m}^{s'_m} \frac{ds}{v_\parallel(s)} = \frac{2}{v}\int_{s_m}^{s'_m} \frac{ds}{\sqrt{1 - B(s)/B_m}}, \tag{7}$$

where s is the arc length along the guiding centre's track and s_m, and s'_m are the coordinates of mirror points. [11]

The approximation holds as long as the bounce period is bigger than the Larmor period with a mostly uniform magnetic field so that along the particle's trajectory

$$\tau_b\frac{dB/dt}{B} \ll 1.$$

2.2   Particle Interaction with Matter

A charged particle traversing matter interacts with the atoms and electrons of the medium via Coulomb force. Incident particles with high energies are capable of interacting with many electrons along their paths. During the interaction, there is a target particle and an incident particle. The target particles can be transferred to higher energy orbitals; this process can excites the particle. The level of excitation depends on the energy of the incident particle. The energy that is released by a photon, corresponds to the orbital energy difference. The incident particle can carry enough energy to displace a target electron from the atom; this process causes *ionisation*. These interactions will slow down the incident particle with each interaction as it loses energy in the ionisation processes. The ionisation level also depends on the properties of the target material. [12] [13]

The faster incident particles move through a material the less energy they lose to electrons. The incident particle can penetrate the target material more as it spends less time interacting with and imparting energy unto the material's electrons. Then, the higher is the incident energy the less is the linear energy transfer. The linear energy transfer for a charged particle much heavier than an electron is described with the *Bethe-Bloch formula*,

$$-\frac{dE}{dx} = \frac{4\pi}{m_e c^2} \cdot \frac{n z^2}{\beta^2} \cdot \left(\frac{e^2}{4\pi\epsilon_0}\right)^2 \cdot \left[\ln\left(\frac{2m_e c^2 \beta^2}{I(1-\beta^2)}\right) - \beta^2\right], \tag{8}$$

where c is the speed of light, $\beta = v/c$, v and z are the velocity and charge of the primary particle, m_e and e are the electron rest mass and charge. I is the average ionisation potential of the material; this value depends on the material. Assuming a non-relativistic regime, equation (8) takes a simpler form with small values for β. The stopping power depends greatly on the target material as different particles lose different amounts of energy to it. [14]

The Bragg curve can describe the the energy deposited vs. depth depth of

the incident particle, where the incident particle loses energy as it advances in the material by depositing energy to the surrounding particles. Eventually, the particle stops and its penetration depth can be assessed by statistical variations of the energy loss. The energy differences can also be directly calculated from Bethe Bloch. [12]. Heavier incident particles lose less energy as the particle moves into the absorber material. Heavy particles decrease their effective charge gradually as they interact with multiple electrons at the beginning of their trajectories through the absorber material. The incident particle can carry enough energy to ionise the target material in *delta rays* or *secondary electrons* as product of the ionisation. Delta rays, in turn, are capable of triggering further ionisation mainly in the absorber material's surface. The trajectory of the incident particles is mainly straight and direct, while electrons have a more curved path through the material. Electrons have a lower energy rate for their energy loss. An electron can lose most of its energy in a single interaction due to its mass proportion with the orbital electrons of the absorbing medium. [12]

Braking radiation or bremsstrahlung is the radiation emitted when a charged particle decelerates or accelerates in an electromagnetic (EM) field. Particles experience changes in their acceleration as they propagate through matter. The energy change for this to happen is released in electromagnetic waves that produce a continuous EM spectrum. Colliding electrons in a hot plasma generate a free-free emission, when charged particles decelerated by a magnetic field cyclotron radiation is formed, and relativistic particles interacting with a magnetic field produces synchrotron radiation. Special relativity effects have to be considered to predict the wavelength accurately from the radiation [15].

2.3   Radiation Environment Around Earth

Around Earth, there is a particle radiation environment that is in constant evolution. This is a complex system where galactic cosmic rays, solar energetic particles (SEPs),

and radiation belt particles interact.

Galactic cosmic rays are high-energy particles that go through space at very high speeds comparable to the speed of light.Cosmic rays consist of 90% protons, 8% alpha particles, around 1% electrons, and 1% heavy nuclei, which are fully ionised [16]. Their sources and energies provide us with a means by which we can study space beyond our solar system. According to theory, cosmic rays are produced by diffusive shock acceleration in supernova remnants and diffuse through all the galaxy [17].

SEPs are correlated with coronal mass ejections (CMEs) and solar flares [18]. CMEs are plasma releases from the Sun's corona in waves of radiation, or solar wind, along with the magnetic field that comes off the Sun's corona. Solar flares release massive amounts of electromagnetic radiation, plasma, and charged particles from the Sun's outer atmosphere. Measuring the flux of solar energetic neutral atoms is vital to understand the acceleration of SEPs and the energetic cost of solar eruptions. Shock waves of coronal mass ejections accelerate SEPs, and their efficiency depends on the presence of suprathermal ions in the corona. When the suprathermal ion density increases, intense waves in the corona are produced; this triggers the SEPs to accelerate while particle scattering strengthens through CMEs [19]. SEPs are a good indicator of solar activity.

Radiation belts are the regions where particles are trapped by Earth's magnetic field. Magnetospheric processes are able to accelerate particle populations locally. These particles are mainly electrons and protons and can be produced by geomagnetic activity when SEPs confine the geomagnetic field. Another trapping mechanism is the cosmic-ray albedo neutron decay (CRAND) process, where some neutrons that are produced by high energy cosmic rays decay into protons and electrons inside the geomagnetic field. The cosmic rays in play have to undergo nuclear interactions in Earth's atmosphere before decaying [20]. The radiation environment around Earth is constantly changing. It is a complex and dynamic system where its

components' energies can fluctuate in short periods of time. [21]

2.4 Magnetosphere

The magnetosphere comprises several plasma populations with different characteristics; there are various properties displayed in its evolution. The different plasmas interact with one another through many types of electromagnetic plasma waves that unfold along the magnetosphere. The solar wind is an essential factor in this evolution, without it, the Earth's magnetosphere would be a magnetic dipole, but its pressuring effects distort it. The solar wind compresses the magnetosphere inward on the Sun's side and pulls it out widely on the opposite side. The solar wind transfers plasma and energy, shaping the magnetosphere. Variations in the magnetosphere's properties are a reflection of the solar behaviour. They can be affected by coronal holes' sources of wind on the solar surface and can also reflect changes in the structure of the solar wind plasma. [6]

2.4.1 Magnetospheric Charged Particles

There are charged particles in the magnetosphere that can be classified as

- $\lesssim$ **10 eV:** in the cold plasma particles

- **1 − 200 keV:** particle populations passing over intermediate energies distinctive of the ring current and the nightside plasmasheet [6].

- $\gtrsim$ **200 keV:** particles in the radiation belts

This classification relies on the subdivision of the instruments that are usually used for different measurements.In theory, different math techniques partly model particle behaviour in the different regions of phase space. In concept, cold plasma consists of ions and electrons drifting at $\mathbf{u_E} = (1/B^2)(\mathbf{E} \times \mathbf{B})$ perpendicular to the magnetic field. [6]

Radiation belt particles drift across the magnetic field. Their drift rates are time-dependant and are functions of the gradient-curvature drift velocity, where u_E is a negligible part in the summation of velocities such that

$$\mathbf{u_g} = \left(\frac{p_\perp^2}{2mqB^3}\right)(\mathbf{B} \times \nabla B) \tag{9}$$

and

$$\mathbf{u_c} = \left(\frac{p_\parallel^2}{mqB^2}\right)\mathbf{B} \times \left(\frac{\partial \hat{\mathbf{B}}}{\partial s}\right) \tag{10}$$

are the relevant terms. In equations (9) and (10) the variables $p_\perp$ and $p_\parallel$ are the perpendicular and parallel components of the particle's momentum relative to the magnetic field $\mathbf{B}$, m is the relativistic mass, the drift direction is determined by the sign of the charge q, and s is the distance along the magnetic field line. Ion and electron populations can be found in the plasmasheet and the ring current [22]. In these kinematic and dynamical scenarios the values of $\mathbf{u_E}$ and $\mathbf{u_g} + \mathbf{u_c}$ are comparable and thus it is important to consider all the velocities as pertinent to the model. Ions and electrons in cold plasma move along $\mathbf{B}$ in gravity-influenced motion that is affected by the centrifugal forces caused by the curvature of $\mathbf{B}$. This motion is dictated by the components of $\mathbf{E}$ parallel to $\mathbf{B}$, while for the plasmasheet, the particles' motion is a function of the auroral arcs. The plasmasheet dynamics, along with the ring-current and radiation-belt particle dynamics, are altered by magnetic mirror forces,

$$\mathbf{F}_\mu = -\hat{\mathbf{B}}\left(\frac{p_\perp^2}{2mB}\right)(\hat{\mathbf{B}} \cdot \nabla B), \tag{11}$$

The resulting dynamics in $\mathbf{B}$ can be bounded or unbounded within the magnetosphere. The particles that are bounded might be so temporarily and are trapped in the magnetosphere. Some particles escape into the ionosphere, others can escape through the magnetopause or into the tail. This process is made possible by particle drift or large particle energies. When the energy is greater than that of the magnetosphere's barrier, the particles break free of their influence. The particles

with enough energy to perform this are the ones forming the galactic cosmic rays and solar energetic particles. [6]

2.4.2 Charged-Particle Motion

$M = p_\perp^2/2m_0B$ is the first *adiabatic invariant* for $\mu = p_\perp^2/2\gamma m_0B$, with $\gamma = m/m_0$, where the relativistic mass is m and the rest mass is m_0. For processes that do not interfere with particle gyration, M is an invariant conserved value in magnetic field lines. Under these conditions, M is proportional to the effect of particle gyration, so that the perpendicular momentum component, $p_\perp^2 = 2m_0MB$, changes in proportion to **B** at the gyration centre. All the electric fields parallel to **B** can be neglected for particles with radiation-belt energies, the parallel to **B** momentum component is described by,

$$p_\parallel = \sqrt{p^2 - p_\perp^2} = \sqrt{p^2 - 2m_0MB} = p\sqrt{1 - (B/B_m)}, \tag{12}$$

where $B_m = p^2/2m_0M$ is the mirror-point field. This point represents the value of B where $p_\parallel = 0$. [6]

Along a magnetic field line, there are points where $B = B_m$ at which charged particles are trapped. The motion of its centre of gyration, or guiding centre, in between the mirror points is the *bounce motion*. The particles' guiding centre takes a bounce period to travel between one mirror point to another and back. When the mirror points are close to the magnetic equator, the bounce motion acts as a simple harmonic oscillator and the bounce frequency is described by $\Omega_2/2\pi = (1/2\pi)(M/\gamma m)^{1/2}(\partial^2 B/\partial s^2)_0^{1/2}$. Here, the subscript 0 denotes the equatorial evaluation, s is along the magnetic field line, the gyrofrequency considered is $\Omega_1/2\pi = (qB_0/2\pi m)$, B_0 is the equatorial value of the magnetic field along a specific field line, and the drift frequency is $\Omega_3/2\pi = (u_g/2\pi r_0)$ with r_0 being the radius of the drift orbit. [6]

α is the local pitch angle between **p** and **B** and the equatorial pitch angle is

$\alpha_0 \equiv \sin^{-1}[(B_0/B)^{1/2}\sin\alpha]$ if the particle is at $B = B_0$ and M is conserved along a specific magnetic field line. The mirror-point field is $B_m = B_0\csc^2\alpha_0$. This value of B_m might not be found at an altitude such that $h \gtrsim h_c \approx 110$ km. When this happens, the particle is in the loss cone. Particles with equatorial pitch angles with $\alpha > \alpha_c$ are trapped as long as they maintain the inequality. When particles have a pitch angle of $\alpha = 0$, they mirror at the magnetic equator. The angle α_c can be calculated with $\alpha_c = \sin^{-1}[(B_0/B_c)^{1/2}]$ where for $L \approx 4 \longrightarrow B_c/B_0 = 100$. The parameter L describes the distance in Earth radii measured from Earth's centre. [6]

The *adiabatic theory of charged particle motion* depends on the frequency separation between spinning, bouncing, and drifting ($\Omega_3 \ll \Omega_2 \ll \Omega_1$) so there is room for an canonical action Hamilton-Jacobi-integral associated with the motion elements ($i = 1, 2, 3$):

$$J_i = \oint_i (\mathbf{p} + q\mathbf{A}) \cdot d\mathbf{l}. \tag{13}$$

The canonical momentum $\mathbf{p}+q\mathbf{A}$ here is comprised of a particle term $\mathbf{p}$ and a vector potential term $q\mathbf{A}$, where $d\mathbf{l}$ is the gyration, bounce, or drift trajectory.

The main ***adiabatical invariants*** are:

- **first:**

  M is defined by convention with expression (13) for the spinning case (i=1) so that [6]

  $$M \equiv \frac{|q|J_1}{2\pi m_0} = \frac{p_\perp^2}{2Bm_0} \tag{14}$$

- **second:** J_2 is the integral of the component of momentum parallel to the magnetic field lines ($p_\parallel$) from one mirror point to the other and back [6].

2.5 Radiation Belts

Particles are trapped in toroidal regions around Earth; these regions are known as radiation belts and boost trapped particle intensity. An accepted explanation for

why radiation belts diffuse and how they are preserved after they were formed is given by the adiabatic theory of charged-particle motion. However, this framework does not provide an explanation for the dynamical processes that dictate the formation and decay of radiation-belt particle intensities. These phenomena involve a weak violation of some adiabatic invariants. It needs to be considered that a particle radiation environment is the product of dynamical processes, and thus, the radiation-belt dynamics must be described in terms of diffusion in space by means of adiabatic invariants in the form of canonical coordinates.

Charged particles experience strong pitch-angle diffusion through which they gain kinetic energy from the transport to the lower values of L. These particles are mainly electrons that precipitate into the atmosphere from the plasmasheet and develop the diffuse aurora. The electron precipitation from the plasmasheet at altitudes where the border between closed and open field lines is is directed parallel to the magnetic field by the electric fields that meet this directional condition and are related to auroral ion beams. These kinds of auroras are discrete arcs that often appear as curtains of light across the sky. Auroral particle precipitation affects electrical properties in the ionosphere through energy displacement that normally ionises the neutral atoms. Auroral activity is boosted when there are magnetospheric substorms present. Abrupt disturbances in Earth's magnetosphere release energy from the *magnetotail*, which is the opposite side of the compressed magnetic field that is constantly oscillating due to the effect of the solar wind . Substorms trigger the injection of energy from the magnetotail into the high latitude ionosphere [23]. Substorms are recurrent phenomena; there can be either storms or substorms depending on their statistics and not their dynamics. In a substorm, the diameter of the auroral oval increases, then there is a sudden contraction of the polar cap radius. While this happens, the band of latitudes between the original auroral oval and the new grown one illuminates. This is the substorm expansion phase, or substorm on-

set, where the illumination spreads towards the poles. On the night-side, the region is thicker in latitude than its counterpart on the dayside because of the asymmetry of the polar cap. The enhanced auroral emission is caused by the precipitation of electrons energised through the induced electric field or by the reduction of Ψ at a specific L. These bands of latitudes that have been formed contain the auroral electron precipitation and its light emission. The precipitation process makes them decay little by little by draining the magnetic flux tubes of the hot plasma from the substorm recovery phase. [6]

2.5.1 Proton Belt

Protons in the radiation belts have energies exceeding 100 MeV; this makes them highly penetrating particles. The proton belts can be located as a function of their energy. At L=1.3, peak fluxes >50 MeV are observed, while lower energy peaks are seen at more distant shells. Protons and electrons have a higher penetration into the terrestrial atmosphere in the South Atlantic Anomaly, which presents a weakness in the magnetic field in the South Atlantic.

Different processes are responsible for proton belt formation. The CRAND contributes to the energetic electron population in the inner belt. Here, the cosmic ray flux arriving at the atmosphere is backscattered as neutrons which then decay into protons and electrons [21]. This phenomenon contributes particles with energies >100 MeV [24]. Earth's magnetic conditions are capable of trapping protons coming directly from the Sun through solar proton events and geomagnetic storms [25] [26]. Radial diffusion transports protons inwardly across the magnetic field towards the Earth [27]. The sourcing processes are balanced by atmospheric absorption, charge exchange with hydrogen atoms, and by Coulomb collisions losses with electrons in the plasmasphere. [21]

At around L=1.7, we consider the inner part of the proton belt, which is very

stable. The particles in the radiation belts are confined in surfaces or *drift shells*. The drift shells are sensitive to Earth's magnetic field changes over long periods of time. These changes produce gradual contraction of the drift shells that increases the proton intensity by a factor of 10 [28]. Planning satellite designs and orbits is closely related to these changes since their repercussions can create hazardous or unsustainable conditions in space. Within the 11-year solar cycle, high solar activity is responsible for the heating and expansion of the upper atmosphere. The condition variability can increase the collision rate and proton losses at certain altitudes, leading to proton flux variation displays in anticorrelation with the solar flux [29]. At $L=2$, more pronounced variations in the proton belt take place during the interaction of an interplanetary shock with the Earth's magnetosphere. Protons of solar origin accelerated by the shock compression of the magnetosphere are able to form a new proton belt in minutes [25]. The proton radiation belt is described in several dynamic models that attempt to reproduce the fluctuations in the outer region where $L > 1.7$ [30] [28].

2.5.2   Electron Belt

An imbalance between acceleration, transport, and loss processes cause electron flux variations in the radiation belts. Electron acceleration takes place in the magnetosphere and there are several models that aim to describe the acceleration mechanisms [31] [32] [33]. The Fermi acceleration is the most accepted explanation of electron acceleration. This acceleration is also known as *diffusive shock acceleration*, and it takes place in collisionless environments where charged particles exceeding thermal energies undergo repeated interactions or reflections. The motion of the particles across the magnetic field on their paths towards Earth can generate the particles' acceleration. The diffusion of electrons towards Earth requires the electron phase space density to increase with L. Observations show that in the inner region at $L= 4.5$, the

particle phase space density reaches a maximum against expected results predicted by inward radial transport which sets this outcome in the outer region. [34][35]. If the conditions are not met, another local mechanism has to be present[33]. Wave-particle interactions can create acceleration locally [36][37]. If so, frequencies are comparable to the electron cyclotron frequency and can resonate with the electrons via Doppler-shifted cyclotron resonance [21]. The adiabatic invariants are broken through this process. The whistler-mode chorus waves are the main wave mode that could contribute to local particle acceleration. The plasmasheet releases low energy electrons that act as a seed population inserted during substorms into the lower L-shells by convective electric fields. The new presence of particles in regions of higher magnetic field strength develops an anisotropic distribution peaking perpendicularly to $\mathbf{B}$. Doppler-shifted cyclotron resonance is then capable of whistler-mode waves. The wave growth is regulated by electron low energy scattering at small pitch angles into the atmosphere. The magnetic field traps high energy electrons that waves resonate and scatter at large pitch angles. Within the magnetic field, at the largest trapped pitch angles, waves resonate and scatter higher energy electrons [21]. Electrons can diffuse to higher energies and boost the flux through the wave power if it is enhanced long enough.

Wave related acceleration can be described in different regions under specific circumstances:

- Between $L=$ 4–6 chorus wave power is most intense at the peak of the outer radiation belt [21].

- Outside the plasmasphere, chorus wave power increases with magnetic activity in regions where electron plasma frequency is considerably smaller than the electron gyrofrequency. These conditions enable efficient electron diffusion to higher energies [33].

- Accelerating waves foresee "flat top" pitch angle distributions which are energy-

dependent and flat between 60–90 degrees that can be seen during magnetic storms [33].

- Some models of wave power consider the bounce averaging and magnetic local time (MLT) variations. They give a timescale for electron acceleration of the order of 1–2 days. This result is comparable to observations [38].

Pitch angle scattering of radiation belt electrons is caused by dominant wave modes, followed by precipitations. These precipitations vary accordingly to magnetic local time. High energy electrons can be scattered by hiss waves (low-frequency waves). The distribution of hiss waves can reach asymmetric standards according to the plasmaphere's shape where they take place. Precipitating electrons are generated through different wave-particle interactions with different wave modes [39]. In the plasmapause, there are waves that scatter electrons into the loss cone [21]. These waves are *plasmaspheric hiss, lightning generated whistlers*, and *whistler mode waves* [40]. The plasmapheric hiss is responsible for the loss at energies from a few hundred keV to a few MeV in the outer plasmasphere [35]. At low L, lightning generated whistlers have a more prominent role. Electromagnetic ion cyclotron waves, at frequencies between the proton and the helium gyrofrequency and between the helium and the oxygen gyrofrequency, are expected to be very effective at scattering radiation belt electrons into the loss cone from the region where the plasmaphere coincide with the ring current [21] [38] [41] [42].

Currently, there is not enough observational evidence to back up the presence of these waves. Further studies are needed to assess the conditions of the radiation belt's environment to describe more complete models of the phenomena present in this region. Electron loss is more pronounced when the electron plasma frequency is more prominent than the electron cyclotron frequency. The study of the plasma parameters is key to improving our understanding of the system. PATE needs to be able to observe electrons coming from other parts of the magnetosphere. To perform
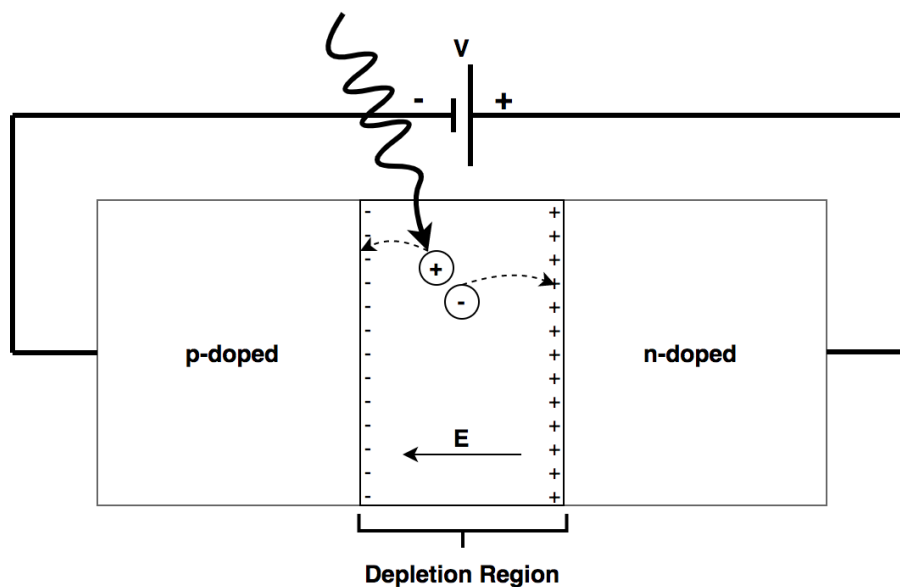
Figure 2.   Shown is a pn-junction with a reverse bias voltage (V). An incident particle impacts the active material and an electron-hole pair is created. Due to the electric field (E), the charge carriers travel to the edges of the depletion region where they will be detected by probes that are sensitive to current.

this task, the orbit needs to be drifting in MLT. To study the loss processes, PATE needs at least one pitch-angle measurements every 15 seconds in the electrons' energy spectra.

2.6   Silicon Detectors

There are several advantages to semiconductor-based particle detectors. In comparison to gas detectors, it is much more compact and space-effective because it is a solid. When comparing to scintillation detectors, it has been shown that semiconductor detectors have better energy resolution [43].

n-doped silicon contains impurities (usually arsenic or phosphorus). The main feature of an n-doping agent is that it has five valence electrons, so when it bonds with the tetravalent silicon atoms, it introduces an extra conduction electron. Similarly, p-doped silicon usually contains either boron or gallium. The main feature of a p-doping agent is that it has three valence electrons, so an electron-hole or va-

cancy is leftover after it bonds to silicon. When a p-doped block of silicon meets an n-doped block, they create a junction where the density of free electrons on either side is discontinuous, and diffusion of electrons from the n-side to the p-side occurs. Since the two blocks were electrically neutral, to begin with, after the charge carriers (negative electrons and positive holes) redistribute themselves throughout the volume, an overall negative charge is achieved on the p-side and an overall positive charge on the n-side. This generates an electric field between the two halves which opposes the diffusion of electrons and holes, and it builds until an equilibrium is reached. This region around the junction point where charge separation builds up, and with it an electric field ($\mathbf{E}$), is called the depletion region (see Figure 2).

Once the depletion region has been formed (timescales of less than a second), it can act as a radiation detector. When a particle impacts the active region, an electron can be promoted to the conduction band, leaving a hole in its absence. In this way, electron-hole pairs are created (see Figure 2), which, due to the electric potential, travel to the edges of the depletion region where their currents can be detected through external equipment. In its current state, it would function as a very poor particle detector. Since $\mathbf{E}$ is small, the charge carriers will not move quickly, and this can result in incomplete charge collection due to two effects: recombination, where a conduction band particle drops down to the valence band, and trapping, where impurities in the material cause the particle to be immobilised. In the case of trapping, particles may escape, but it may not be until much later, and it will not be counted towards the detection pulse. These processes happen on a timescale of $\approx 10^{-5}$s, so the electric field needs to be large enough to cause migration to the edges of the junction in $\approx 10^{-7}$s or 10^{-8}s. [44]

In order to make an efficient detector, one needs to increase the width of the depletion region for more active volume and increase of speed of mobile charge carriers. One can accomplish this through the use of a reverse bias; this means

that the n-side is connected to the positive terminal of a battery, and the p-side is connected to the negative terminal of said battery (see Figure 2). This has the effect of increasing the electric field and expanding the depletion zone. The new depletion width would be

$$d \simeq \sqrt{\frac{2\varepsilon V_0}{eN_I}}, \tag{15}$$

where ε is the permittivity of the material (silicon), V_0 is the external applied voltage, e is the elementary charge, and N_I is the impurity concentration.

Increasing the voltage is advantageous in multiple ways: it increases the width of the depletion region, increases charge carrier mobility and decreases the capacitance, all of which contribute to enhanced energy resolution. [44]

The critical value of voltage that leads to d expanding to the backside of the wafer is the *full depletion voltage*,

$$V_{fd} \simeq \frac{d^2}{2\varepsilon\mu\rho}, \tag{16}$$

where d is the detector thickness, μ is the mobility of electrons in n-type bulks or holes for p-type bulks, and ρ is the specific resistivity of the bulk. When the depletion voltage is reached, the full volume of the detector becomes active detection material. [45]

The energy needed to generate an electron-hole pair is called the ionisation energy (ϵ). This energy is inversely proportional to temperature, its value depends on the type of particle involved in the interaction, and some research suggests it also depends on the energy of the incident particle [44]. For our purposes, the energy a particle deposits in the depletion region is given by the following equation

$$E_{\mathrm{deposited}} = N\epsilon, \tag{17}$$

where $E_{\mathrm{deposited}}$ is the energy deposited by the incident particle and N is the number
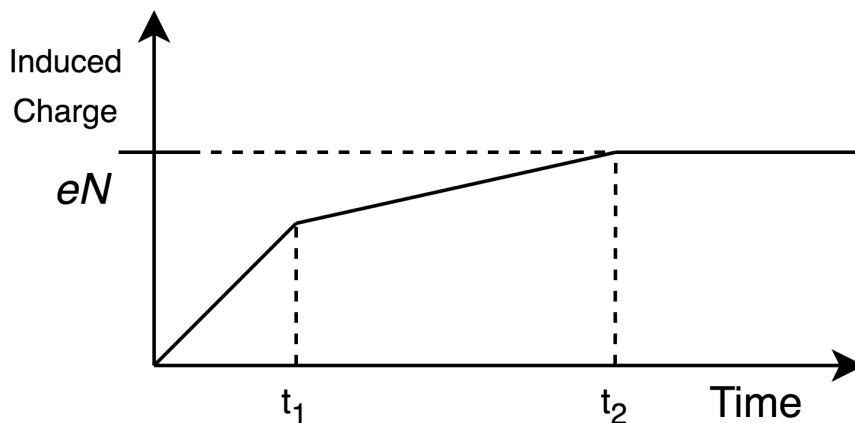
Figure 3. t_1 represents the collection time for particles that are registered first (can be either electrons or holes). t_2 is the collection time for the second particle type. Assuming no loss due to trapping or recombination, the resulting pulse will be generated from a charge of eN, where N was the number of electron-hole pairs generated by the event and e is the elementary charge. [44]

of electron-hole pairs created. Since it is possible to measure the current and the current is related to N and other known parameters via the relation

$$I \equiv NeAv_{\text{drift}}, \tag{18}$$

where A is the area through which the charges pass, and v_{drift} is their drift velocity, we can solve for N and find the energy of the incident particle. The ionisation energy of silicon takes on a value of 3.62 eV at 300 K, and the mobility of holes and electrons through silicon is also known to be $\approx 480\text{cm}^2/\text{V}\cdot\text{s}$ and $\approx 1350\text{cm}^2/\text{V}\cdot\text{s}$ respectively at 300 K. The hole mobility tends to stay within a factor of two or three times less than that of electrons. [44]

Other factors to consider include the energy lost in the dead layer which is the material the incident particles have to traverse before reaching the active volume. This energy loss is proportional to the thickness of the dead layer and related to the angle of incidence [46]. There exists what is known as a leakage current that arises from the small conductivity that the semiconductor has and acts as background noise. Lastly, there are two different currents that lead to a signal in the detector:

the electron current and the hole current. As previously discussed, they move at different speeds, and the distance they need to travel to get to either edge is likely to be different. As a result, one must consider two pulse collection times that make up a single detection (Figure 3) [44].

3 FORESAIL-1 and PATE

The Finnish Centre of Excellence for Sustainable Space plans to develop a series of missions, the first of which is FORESAIL-1. FORESAIL-1 is scheduled to embark on a mission to the polar low Earth orbit. This mission should characterise the electron precipitation from the radiation belts, and give insight into ENAs coming from the Sun and those observed during strong solar flares. The FORESAIL-1 mission includes a 3-units CubeSat, a standard design for nano-satellites whose structure can be scaled in cubes with 10 cm edges and a mass of less than 1.33 kg. FORESAIL-1 transports a particle telescope (PATE) to measure energetic protons at 0.3–10 MeV in ten channels and energetic electrons within a nominal range of 80–800 keV in seven energy channels. Higher energy particles with enough energy to penetrate the whole device will be measured in one >800 keV electron channel and two integral proton channels at >10 MeV energies. FORESAIL-1 carries PATE and a Plasma Brake (PB). PATE is in charge of the particle measurements, while PB is a tether experiment used to decrease the spacecraft altitude. The plasma brake allows us to achieve the requirements of getting particle measurements with a drifting MLT. [4]

PATE fosters two telescopes perpendicular to one another. This system allows one of the telescopes to measure along the spacecraft's spin axis while the other covers the perpendicular region. The rotation axis points at the Sun to measure the energetic hydrogen while the second telescope scans the pitch angle distribution of charged particles. A spin period takes 15 seconds nominally; during this time, the rotating telescope can provide angular distributions of electrons and protons at +11.25°resolution. This information can help calculate the pitch-angle distribution and distinguish between trapped and precipitating particles.

The conditions allow one to observe main solar energetic particle events like the one recorded in December 2006. A burst of 1.6 to 15 MeV ENAs from the Sun was

observed, apparently produced by either flare or shock-accelerated protons [47]. The two telescopes working together provide comparing rates, and the geomagnetic field works as a filter to create the conditions needed for these observations. Simulations are essential to verify the performance of the angular response functions under the expected energetic conditions and to check the sensitivity levels needed to make the measurements.

FORESAIL-1 will face space conditions related to the magnetosphere. Many different satellites work together to make observations that will provide us with an overall panorama of the possible conditions FORESAIL-1 may encounter. The measurements will be performed under different environmental conditions, especially in the critical observation regions. FORESAIL-1 will measure the energetic particle precipitation cone from these sources and the radiation belts. Collaboration with other projects is also essential in the analysis to assess wave activity in the magnetosphere. The satellites can monitor the substorms occurring in the magnetotail and the fast earthward plasma flows. The observation's interpretation relies on this information.

3.1   PATE Objectives

The structure of the belts has previously been discussed. We mainly have to consider the energetic protons that remain in a quasi-stable state in the inner belt and the energetic electrons that produce a highly dynamic system in the outer belt. The outer belt starts around L = 3; the most intense activity occurs between L = 4 and L = 5. It is here where the magnetic field lines correspond to 60°-65°magnetic latitudes. [48]

The mechanism through which relativistic electrons in the radiation belt acquire their energies is yet to be studied. These electrons present energies between 600–700 keV up to tens of MeVs. They are transported in and out of the belts. They ulti-

mately escape through the day-side magnetopause or towards the upper atmosphere by wave-particle interactions with local pitch angle scattering. Thus, the processes that take part in these dynamics cover a large spectrum of energies from keV to relativistic energies.

The satellite provides bus supplies of around 2.5 W of almost continuous power consumption of PATE. PATE's duty cycle is related to the observations' coverage: the latitudes in the outer belt region and the low-latitude region outside of the South Atlantic Anomaly (SAA). To get particle measurements under a drifting MLT, it also carries a plasma brake to control altitude. PATE stays in its original orbit for four months to scan the different pitch angles of the spacecraft spin while the satellite's spin is aligned to the meridional plane. This orbit provides Sun-synchronisation for an altitude beyond 600 km. After the initial phase, a plasma brake will decrease the altitude by 100 km approximately, which will alter the MLT drift. In the following months, the device would be in preparation mode for the observations. The PATE spin axis will be facing the Sun for the nominal observations. The Sun pointing is a non-inertially-fixed direction that cannot be kept with a deployed tether. [48]

One of PATE's main concerns is to cover the most extensive energetic range possible. Pitch-angle resolved measurements are necessary to study particle precipitation into the atmosphere. Electrons that precipitate at ~100 km have enough parallel energy to avoid mirroring before hitting the atmosphere when their pitch-angles are sufficiently small. The field lines dictate the local loss cone width, making it wider towards Earth. When considering the dipole approximation, the loss-cone boundary is somewhat independent of L in spherical polar low-Earth orbits [48].

Precipitations from the belts are expected to show different behaviours depending on the type of solar wind transients that trigger reactions through interactions with the magnetosphere. Solar wind can be characterised by its sources, such as coronal mass ejections, shocks, sheaths, slow-fast solar wind streams, and fast streams.

These sources can be studied through other satellites; their observations can help analyse PATE's data. The resulting precipitation can be quantified through the solar wind details, while geomagnetic activity can be studied through long observational periods of about six months. This time window would allow the device to detect different solar wind structures that have an impact on Earth. [4]

3.1.1 Instrument's Description

FORESAIL-1/PATE is comprised of two telescopes: T1 and T2, with identical stacks of silicon detectors under collimating structures. T1 is set perpendicular to the spacecraft's spin axis, and T2 is aligned parallel to the spin axis. The collimated structures for T1 and T2 have different lengths: T1 is longer than T2. The device weighs 1.2 kg and has a physical volume of $94{\times}94{\times}140$ mm^3. [48]

The main similarity between the telescopes, T1 and T2, is the stack of three silicon detectors that can stop particles in the nominal range of the instrument:

- D1~ *20 μm*

- D2~ *350 μm*

- D3~ *350 μm*

The nominal range comprises 80–800 keV for electrons and 0.3–10 MeV for Hydrogen. The D detectors are just a part of the device; there are also anti-coincidence (AC) detectors AC1 and AC2. A visual representation of the detectors' shapes is shown in Figure 4. AC1 has a hole in the middle that controls the aperture of the instrument. This part is positioned at the top of the stack participating in the collimation process. It actively limits the incoming background particles from being detected. AC2 is a disc at the bottom of the pile that signals the particles entering the structure from the backside. The detector has an upper shell of double nickel foil that keeps low-energy charged particles and soft x-ray photons away from the
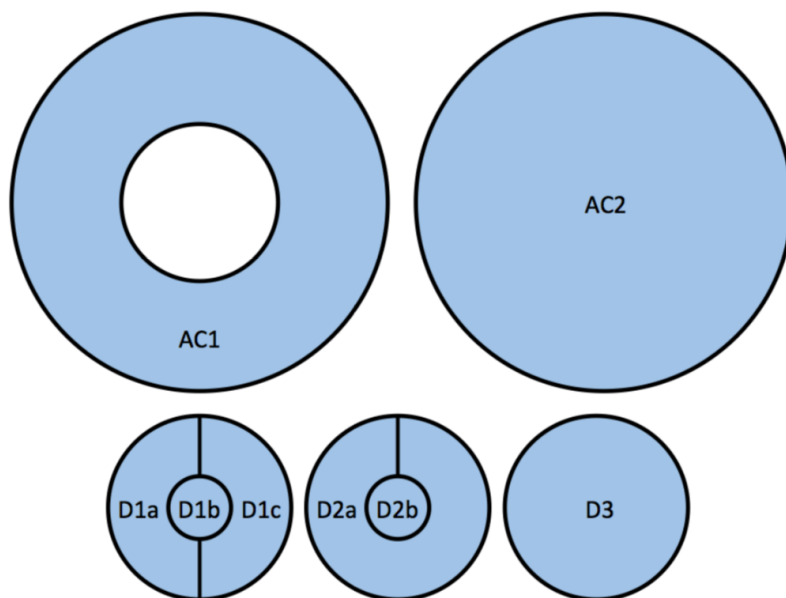
Figure 4. Segmentation of the PATE detectors. Image credit: Oleynik et al. [48]

detectors. The foil is vulnerable to micro-meteoroid dust particles in orbit. Thus, a double layer was implemented to keep the device protected even in the event of tiny hole formation. [48]

The overall layout is made out of several different detectors. Each of the detectors is attached to their Printed Circuit Boards (PCBs) which contain the electronics that control the voltages. These systems are responsible for the guard ring and filtering which provide the voltage needed via resistors and capacitors. The detectors are bonded with an aluminium wire of 25 μm, which allows 1 mm of separation between them; the whole stack measures around 1 cm in height. The voltages are supplied through coaxial cables that bring the signal to the pre-amplifiers. When the signals reach the pre-amplifier board, they continue to the signal processing board. The signal processing board is in charge of digitising the signal at a 14-bit accuracy. The field-programmable gate array (FPGA) receives the digital signal and determines the particle type and energy range that it falls under. The sub-classifiers' combinations for a valid hit criteria are shown in Figure 5. [48]

The FPGA is a major component of the detector; it is responsible for the scientific

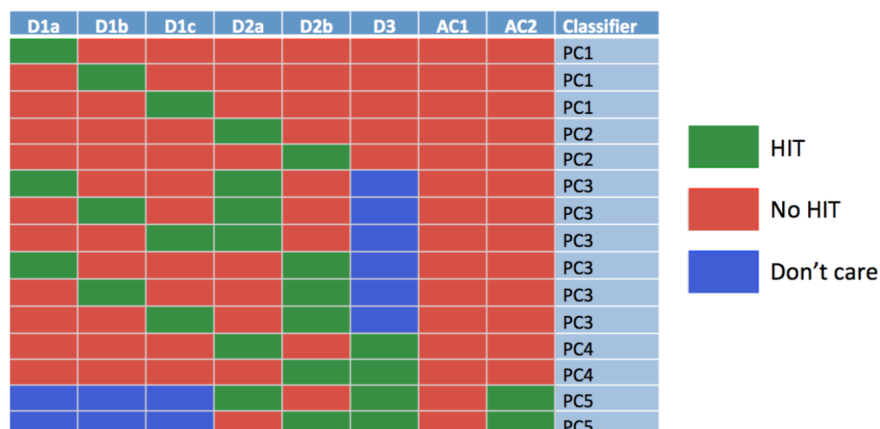| D1a	D1b	D1c	D2a	D2b	D3	AC1	AC2	Classifier
								PC1
								PC1
								PC1
								PC2
								PC2
								PC3
								PC3
								PC3
								PC3
								PC3
								PC3
								PC4
								PC4
								PC5
								PC5

Legend: HIT, No HIT, Don't care

Figure 5. Sub-classifiers' combinations for a valid hit criteria. Image credit: Oleynik et al. [48].

data path. A *trapezoid filter* filters the digitised 14-bit wide data stream of each signal symmetrically. The output of the trapezoid filter preserves uniformity in the data width inside the data path by saturating it to 14 bits. The output is compared to the threshold value; if it exceeds the value, a hit is detected in the *pulse detector*. The detected pulse has a height that is sent to the *particle classifier*. The hit information and pulse heights from all of the detector plates are used to make an energy scale conversion. The energy scale results and energy-loss proxies used in the classification method. The particle classifier has five sub-classifiers, PC1, PC2, PC3, PC4, and PC5. Each of them has its own role in recognising each of the hit combinations. [48]

Particles are classified by the energy they deposit along their paths through the different layers of the detector. PC1 classifies particles that halt in the D1 detector into proton bins. PC2 classifies particles that only produce a pulse in D2 into electron bins. PC3 is concerned with particles that cause a pulse in D1 and D2. For this case, the classification is carried out based on their combined energies and thus can ultimately be classified as an electron or proton. PC4 verifies pulses in D2 and D3 but only assigns electron classification. Finally, PC5 classifies particles that go through the whole stack of plates and has the aptitude to classify particles as either

electrons or protons. The signal path is therefore composed of three main parts and processes: the *trapezoid filter*, the *pulse detector*, and the *particle classifier*. They all have main clocks; the first two have clocks of ~10 MHz and the latter of ~40 MHz. [48]

There are seven energy channels for electrons and ten for protons in the nominal energy range generated by particle classifiers, and three penetrating particle channels in PC5. The time resolution of the measurement is the same as the rotation period of the satellite (15s). T1 will deliver the counts in 32 angular sectors per rotation when scanning the sky. In this way, a full pitch angle distribution will be provided every spin period [48].

In the first detector on top of the stack, D1, there is an efficient separation and sorting of particle species. Proton and electron channels can be contaminated by electrons and protons, respectively. There is some probability of the channels being contaminated by the wrong particle species in narrow energy bands. PATE has separated channels for electrons, so the possibility of electrons contaminating proton channels in this detection area should be considered. It is also possible for the contrary to occur, and protons can pass through passive regions of D1 without triggering a signal. The protons can have around 1 MeV, and it is not possible to tell them apart from electrons with the classifier. PATE could register them as electrons in the lower channels. It is essential to rely on channels to store the different kinds of species to mitigate the contamination between channels sourcing from the detection process in the detectors. These contaminants can be reduced from the data and avoid channel contamination. Aside from protons and electrons, PATE can be subjected to other particles capable of contaminating the measurements in the space environment.

3.2 Simulation

PATE's simulations involved a Geant4 model that includes a geometric description and a mechanical representation of the device.

To enhance the effectiveness of the simulations, some components were removed from the model, such as thread structures and electronic components. The difference in performance without the mass of these parts is not relevant for the stopping power of the instrument. The active volumes concerned with the detection are described physically as simple shapes such as cylinders and prisms. Other parts are also described logically with these shapes. The lack of round edges improves the background noise management as it decreases the uncertainties that they can originate. The particles in the simulation have their momenta calculated by the uniform Lambertian angular distribution, which depends on the angle relative to the normal that is perpendicular to the surface of the source.

The signal processing is linked to the signal path. The model includes a trapezoid filter and pulse detector for signals from a generic detector with a capacitance between 100-500 pF. ModelSim synthesised the totality of the data path and the particle classifier. [48]

The simulations were carried out in two modalities. The calibration modality sets a controlled beam in controlled lab conditions to verify the response of the detectors and compare it to a real-life scenario where the targeted particles are known. The signals obtained are analysed to distinguish between electrons and hydrogen. The test also measures particle energies, as it would happen in the FPGA. The sorting criteria for the simulation place the particles exclusively producing a hit in D2 ($>$50 keV) as electrons, and if the hit is only identified in D1, they are considered to be hydrogen. Other lesser values can also be considered. However, lower values in other active materials (D1a, D1c, AC1 and AC2) are usually within the background noise range. The second modality sets the conditions under which the detector is

expected to perform. The conditions out of the atmosphere are known to be a harsh environment for instruments. The simulations carried out during this modality corroborate the detector's performance and its ability to detect the different range of particles accurately.

3.2.1 Testing Facility

To carry out the first modality, a series of tests were made at RADEF. The RADiation Effects Facility specialises in technologies related to nuclear physics and accelerators. It provides a means to study radiation effects in electronics and devices such as PATE. RADEF operates within a wide radiation range, from gammas and electrons to protons and heavy ions.

In Figure 6, there is a scaled diagram of RADEF's layout and the beam's path in it. RADEF has two irradiation stations along with an electron accelerator (LINAC) and a control barrack. RADEF can produce different beams in different scenarios: proton irradiation in air, low-energy proton irradiation in vacuum, and heavy-ion irradiation in air and vacuum. The beams produced are thoroughly measured, the beam flux and uniformity is assessed by 300 μm thick silicon detectors. There is a collimator system that fixes the tubes. The beam composition is checked with the energy spectrum. [49]

The main beamline path leads to a vacuum chamber; here, some tests are carried out in a vacuum environment that prevents the spread of particle energy, especially for low-energy proton tests. Heavy-ion tests can be carried out in a vacuum or in the air. Inside the vacuum chamber, a remotely operated device holding platform moves the device under test (DUT) in front of the beam. There is also a beam collimator available to restrict the irradiation area on the device. The device can be moved horizontally and vertically through the axis, but it is also possible to tilt the vertical axis with a linear movement apparatus (LMA). [48]
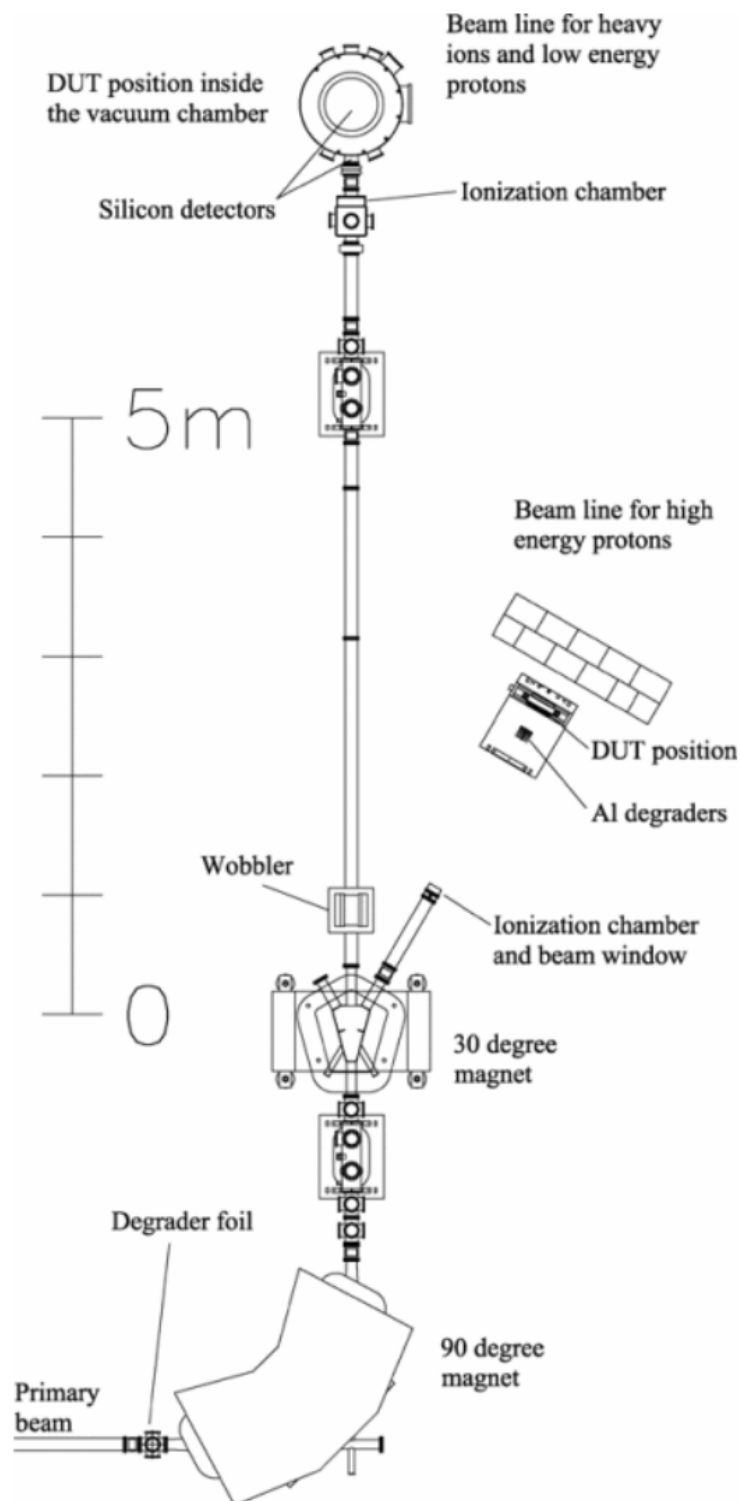
Figure 6. RADEF facility description diagram with beam line layout. Image credit: [49].

3.2.2   Calibration

For PATE's trial, RADEF's cyclotron generates a beam that takes two hours to stabilise. The main narrow monoenergetic beam passes through a degrader and a magnet awarding it arbitrary particle energy. Wobbler magnets can achieve good beam homogeneity; a XY-wobbler changes a focused beam into a wide uniform beam in a dynamic process. There are silicon detectors near the DUT that control the beam energy.

For the calibration campaign, two beams were studied.

- For the first trial, a **10.5 MeV** primary beam was used. The angular response was observed from +15 degrees to -11 degrees with a 200 µm aluminium degrader on the primary beam.

- For the second trial, a **55 MeV** primary beam was used. 5.5 mm and 8.5 mm aluminium degraders provided approximately 40 Mev and 30 Mev resulting energy, respectively. The primary beam help determined off-axis contamination. The degraders were used with different angles (0, +45, -45, +88, and -88 degrees). This energy beam's objective was to observe the penetration of protons from the side of the detector and was not used for calibration.

The observations for both energies were carried out with the full stack of detectors and the short tube of the instrument. The test was carried out in the vacuum chamber, which also offers the rotating table to move the device inside it. An optical camera is available inside to assist the beam direction.

For the Geant4 simulations, the facility was recreated. The materials and geometry include the detector's components but also the facility's conditions. It includes the beams and the short tube of the PATE instrument. The layout includes an aluminium degrader that is included as an aluminium plaque. In the simulation, the primary beam energy is 10.5 MeV. Geant4 offers a display with a simple interactive
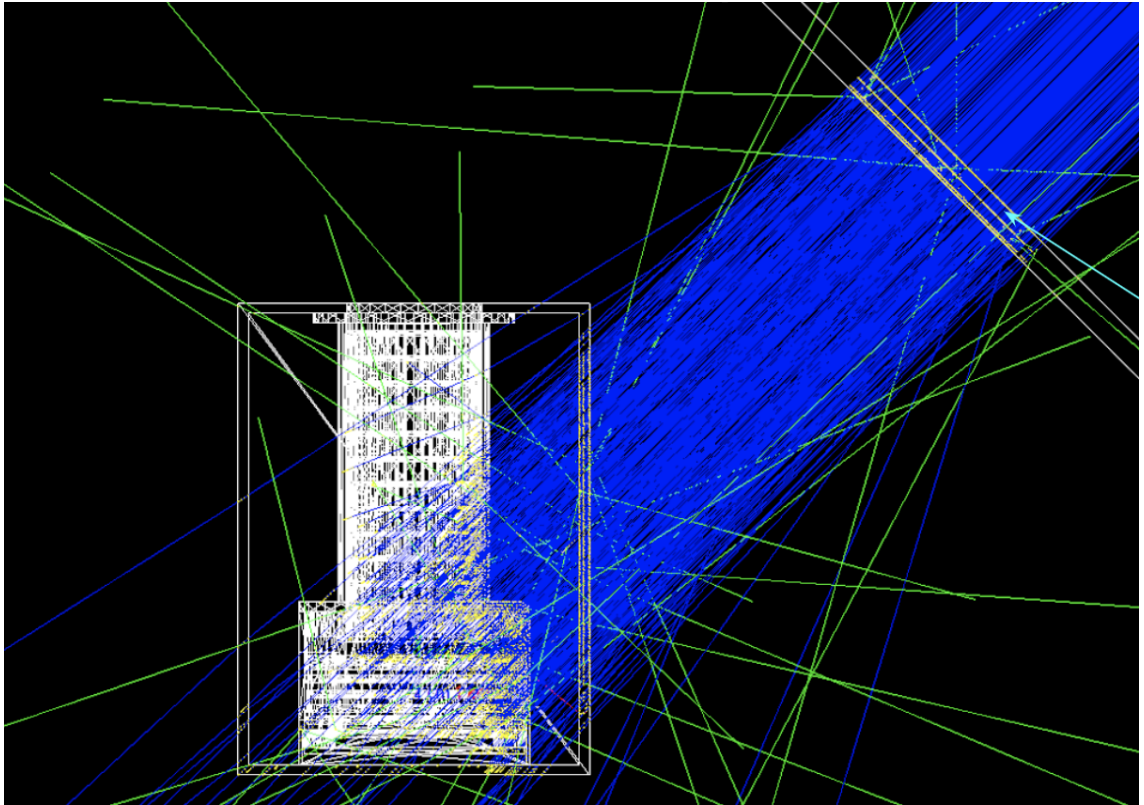
Figure 7.   Geant4 display of PATE's simulation in RADEF facility of a proton beam with an energy of 55 MeV. PATE is shown in white, and the aluminium plaque can be observed at the upper right corner pointed to by a cyan arrow. In this image we can observe protons in blue, gammas in green, and electrons in red. Image credit: Philipp Oleynik.

interface that allows us to see the simulated device from different angles and the particles' paths and interactions. In Figure 7, it is possible to see the 55 MeV beam made out of its individual particles: protons are blue, gamma rays are green, and electrons are red.

4 Results

The results are divided into two sections. The preliminary section presents the data and information provided before the analysis of this thesis took place. Here, the results from previous studies are gathered and discussed. A more detailed explanation of the methodology used in previous studies is included, and their results are presented. The work of this thesis was limited in this section, and it is bounded to the selection of the data considered. The simulated response section includes a more detailed description of the scope of this thesis. Here, the methodology and procedures taken to obtain the results are reported, and some of the immediate outputs are briefly assessed.

Geant4 simulations had the RADEF set-up and helped assess the geometry experiments carried out in 2020. The instrument provided raw pulse-height data and particle counters. The pulse height data came from the simulations' efforts to match the instrument's performance with the given model. The electrical signal converts something we cannot measure into something we can measure, and the simulations guide the measurements and test the performance reliability. However, the comparable results need to be analysed and interpreted as noticeable differences with an explanation can improve the set-up, simulation, testing, or understanding of the device.

Hit patterns present differences from the simulated ones as shown in Figure 7. The particle statistics on plots show slightly different results and cannot be normalised to each other. These discrepancies in the histograms may be pointing to an alignment error during the testing at large angles. However, the simulation results give a clear panorama of the expected response. Given the very precise nature of the test, a slight angle disparity may present a very different view from what was expected. The calibration is carried out on the axis response of PATE with a dense array of beam energies. The selected energy spectra assess the angular response.
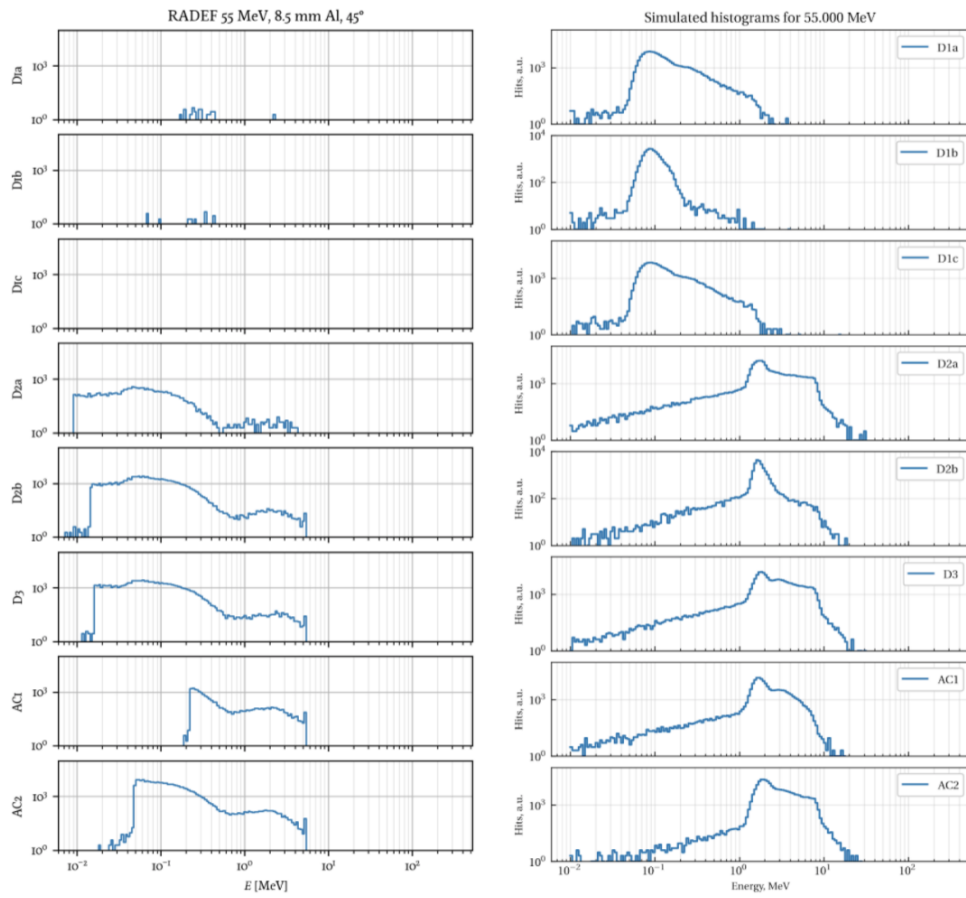
Figure 8. The right side panels show the measured hit patterns and the left side corresponds to the simulation results for the 55 MeV beam.

PATE's field of view is determined by the particles inside the nominal energy range, beyond that, the angular response becomes broader as the collimating structures lose their effects on the particles.

4.1 Preliminary Calibration Data

In this section, the results from the first calibration modality are analysed. During the RADEF trials, two beams were tested: 10.5 MeV and 55 MeV. For our purposes, we focused on the 10.5 MeV data and checked the histograms of the hit count for different energies. When compared, the simulated results and the measurements of the RADEF beam showed that the patterns in the histograms did not perfectly overlap.

Simulations were carried out with a 10.5 MeV beam at different angles, with and without a 200 μm aluminium degrader. The beam energy and the degrader were set in the experimental layout and the rotating table determined the different angles. The data available from RADEF includes a variety of angles and energy combinations with the degrader. These measurements focused on the energy-hit histograms and were carried out with the 10.5 MeV beam.

The hit histograms fill out the energy range considering a thousand hits regardless of the number of hits registered to avoid cramped results and have a better comparison margin with the simulations. The histograms were laid out by the detecting areas: D1a, D1b, D1c, D2a, D2b, D3, AC1, and AC2, as shown in Figure 4. D1c was damaged during the testing measurements, so the data for this detection area were not gathered.

During the detection, we had to consider the stacked up nature of the detector. All the discs and rings are one on top of the other, making AC1 the uppermost disc followed by D1. There are particles, such as protons, capable of going past one or two rings. The rings can act as additional degraders, and we have to consider that

D1a = 1.4	**D1b** = 0.162	**D1c** = -
D2a = 0.842	**D2b** = 0.776	
	D3 = 0.76	
	AC1 = 0.91	
	AC2 = 0.972	

Table I. Gain values per detection area used in the histograms. The units are MeV/1000 instrumental digital values. These values were calculated before the work of this thesis.

when there are energised protons: the more energy they have, the less energy they deposit. Incoming protons lose some energy in the rings that can be observed in the histograms. We have to consider the device's limitations and electronic systems. The electronics might not have a good enough reaction time, and there might be overflows or false piling ups. To avoid this, we can turn off the ring parts of the detector's discs and leave just the central area. In this configuration, it acts like a slightly different instrument in that the collimation process changes, and the left area is around one order of magnitude smaller. The count rate in the detector can be limited; D1b and D2b are responsible for the lowest energy ranges in the spectrum for protons and electrons. There is a power-law-like spectrum in the energy range that is more abundant, in which each step in energy reduces the intensity. A geometric regression is set by the power law, making the particles that reach D3 not so abundant. High fluxes carry out the segmentation. It is important to analyse the beam data of both the central and outer ring to test the response performance of the detector.

The calibrated gains were predetermined with simulation and performance data. Gains are the connection between energy (in MeV) deposited in the detectors and the digital value we obtain during the instrument's detection. The gain values presented in Table I had been checked beforehand but are still being verified and studied. The gains show how much energy is deposited in each detector. The observations were stored in arrays that contain the record of the events. Each event count was

triggered when overcoming a determined threshold. This work is a verification of the gain values by relating the simulated response of the detectors and the measurement data gathered at RADEF.

4.2   Simulated Response

In this section we discuss the follow-up analysis after the preliminary results presented in the previous section. Comparative criteria are introduced and assessed to relate the hit histograms' results of the simulations and of the RADEF test measurements. We describe the steps taken in the calculation of the detectors' gain ratios and report the outcome for each of the steps. Some consequences of the methodology are described and the solutions provided are explained and argued. Follow-up actions are deduced from the analysis conditions and its output. This section details the steps taken in the data analysis for the verification of some aspects of PATE's performance during the RADEF calibration campaign. It focuses on the individual detectors' performance regarding their energy ranges, hit counts and gain ratio calculations.

The right-panel histograms in Figures 9, 10, 11, 12, and 13 show RADEF data already given in units of MeV, that is to say, the pulse heights had already been converted to energies via the aforementioned gain values. If one then compares the distinctive peaks of the simulated response (in MeV) to the measured response (also in MeV) (see Figure 13) by plotting them on the x- and y-axes respectively, one can determine the relationship between newly measured gains and previously measured gains. In other words, if one assumes that the points on the simulated and measured histograms are indeed analogues of one another, one would be assessing the fit given by the equation

$$G_0 P = A \Delta E, \tag{19}$$

where G_0 is the prior gain value, P is the pulse height measured by the detector, ΔE is the simulated peak energy, and A is the fit parameter i.e. the ratio of the previous and new gains. ΔE can also be rewritten as the product of a gain with a pulse height. Equation (19) can then be expressed as

$$G_0 P = APG_1, \qquad (20)$$

where G_1 is the newly calculated gain.

$$A = G_0/G_1, \qquad (21)$$

where the closer A is to 1, the closer the agreement between the two gain values is.

The histograms presented are compared in pairs of Simulation/RADEF with the same energy beam and degrader. The pairs were determined by comparing the histograms' shapes and energy peaks. The data histograms set the parameters for the comparisons. Simulations were carried out by taking in mind the available observations from the RADEF measurements. The data gathered included observations for 0°, 2°, -2°, 5°, -5°, 7°, -7°, 9°, and -9° with a 200 μm aluminium degrader. The matching process just compared the data histograms for a certain angle (the negative and positive counterpart) and contrasted it with the histograms of the simulations for the corresponding positive angle and the simulations in a ±2° range. For example, the RADEF measurements provided histograms for 5° and -5° angles. These histograms were compared against the simulation histograms of 2°, 3°, 4°, 5°, 6°, and 7°. Most of the pairings respected the angular parameter and were matched to their corresponding angles. No angular offset was found by comparing the results, however, some RADEF testing measurements resembled better their negative angular counterparts, especially for larger angles. Only one measurement without a degrader was considered while the rest had a 200 μm aluminium degrader.

In Figures 9, 10, 11, and 12, the pairings of the simulation and the measure-
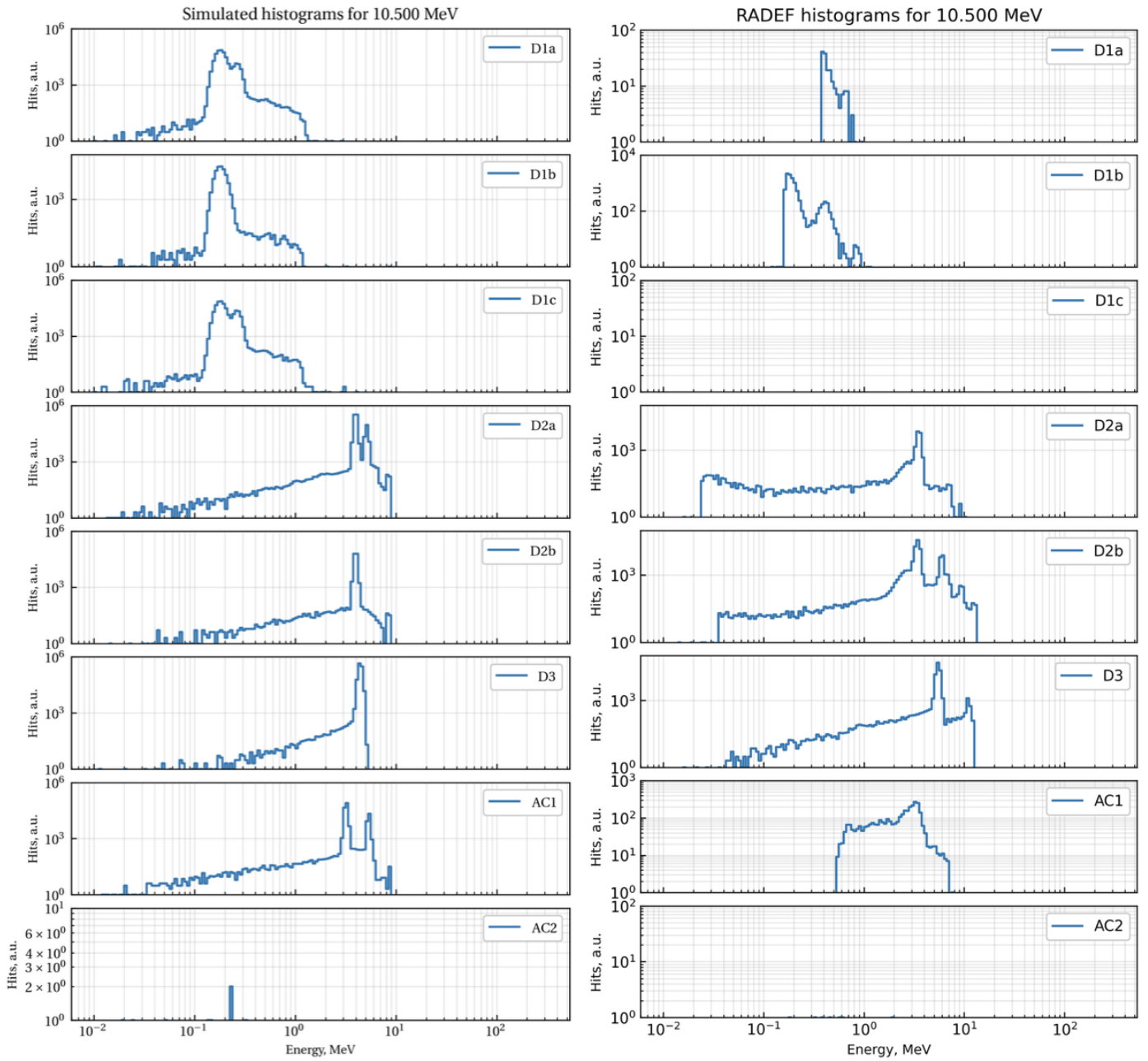
Figure 9. Histograms for the 2° angle with a 200μm aluminium degrader during the 10.5 MeV beam simulation (left) and RADEF test (right).

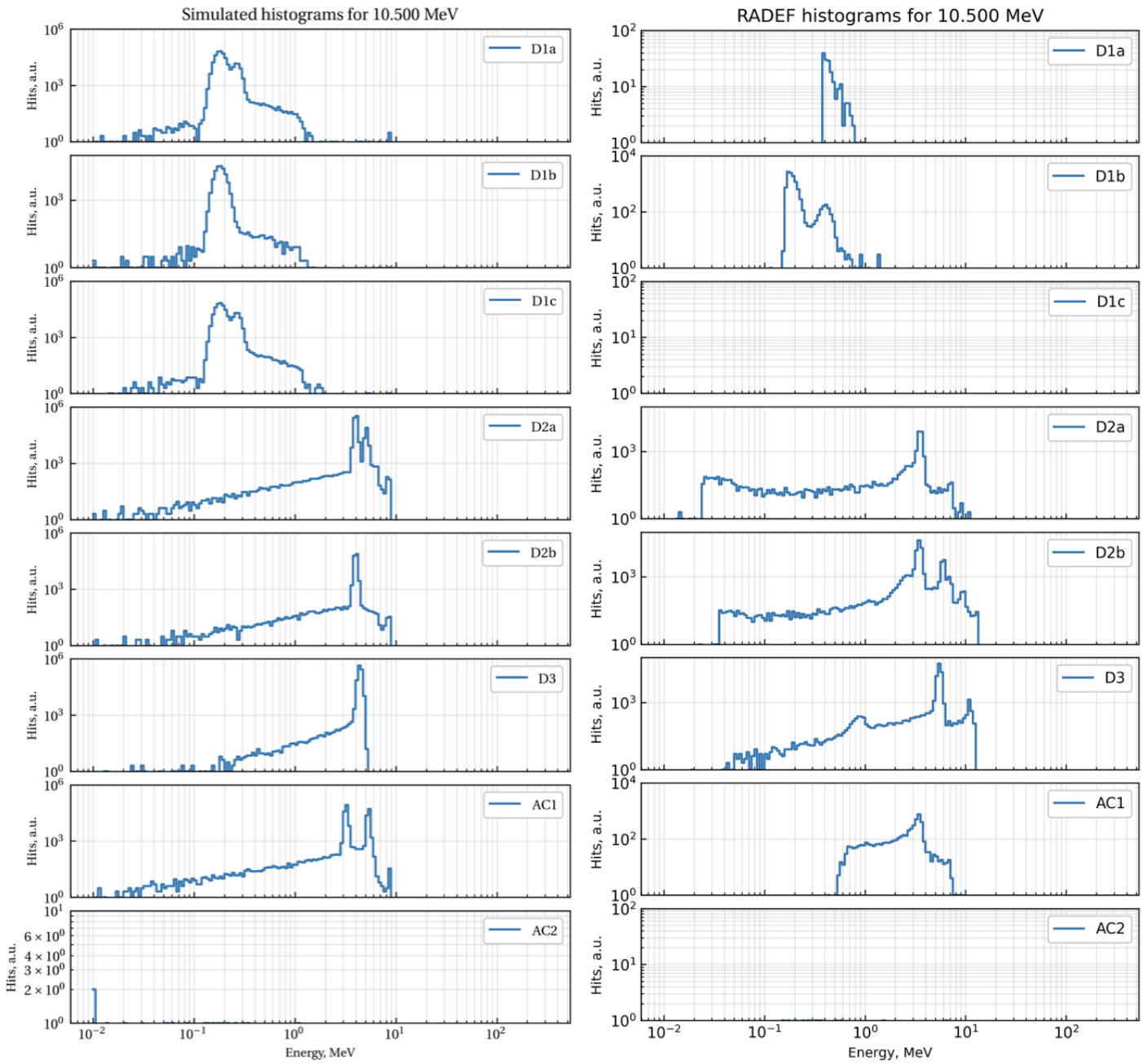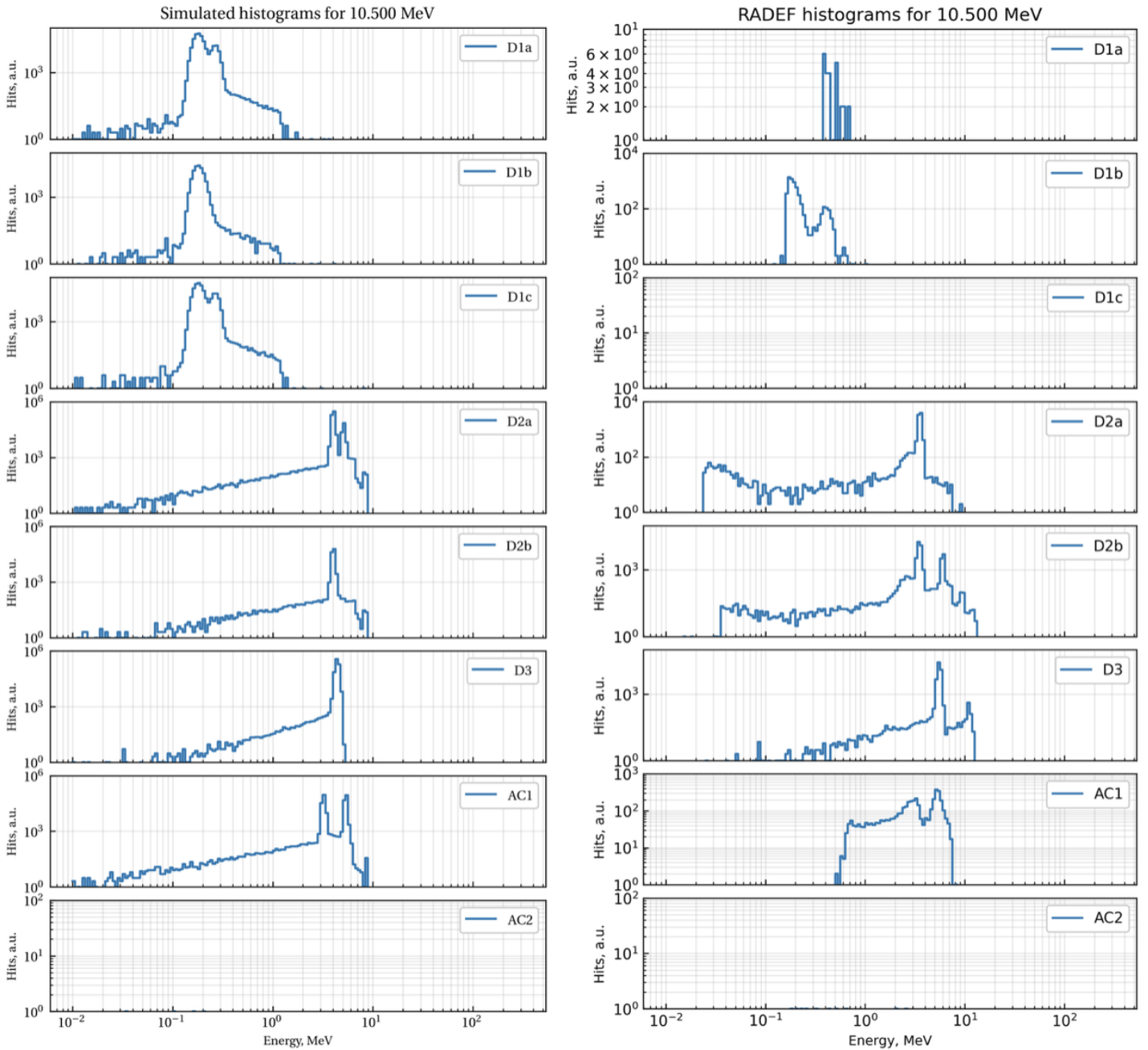Figure 10. Histograms for the 5° angle with a 200μm aluminium degrader during the 10.5 MeV beam simulation (left) and RADEF test (right).

Figure 11.   Histograms for the 7° angle with a 200μm aluminium degrader during the 10.5 MeV beam simulation (left) and RADEF test (right).
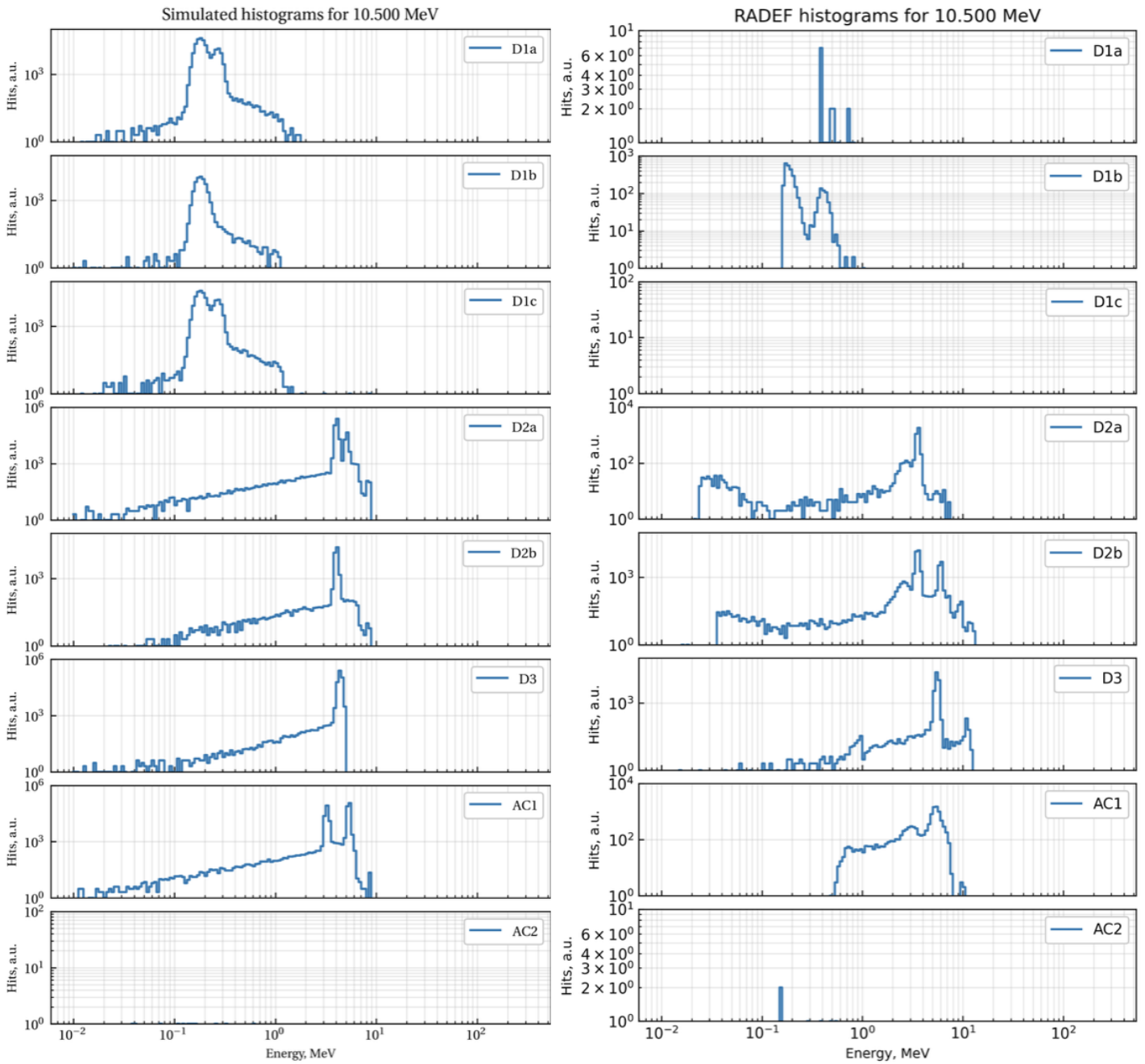
Figure 12. Histograms for the 9° angle with a 200μm aluminium degrader during the 10.5 MeV beam simulation (left) and RADEF test (right).

ments are shown. The RADEF histogram variety included their negative angular counterparts, while the simulations gathered a more detailed angular sample that could adapt to the data information. If more samples were needed, it was possible to run more simulations with more specific angular conditions.

The zero degree angle histograms were also considered with and without a degrader to aid in determining peaks. Thus, the histograms show a series of peaks that can be easily spotted. The main ones were selected for all the compared figures and matched manually with their counterparts. For each histogram set in either simulation or measurements a peak-finding algorithm was employed. The algorithm located the XY values of the peaks present in the histograms. The function takes a 1-D array and finds all the local maxima by comparing neighbouring values. Additionally, an extra condition was set to locate the peaks above 150 hits to reduce the number of local peaks and pinpoint the global peaks.

In Figure 13, it is easy to notice that the simulation results threw fewer peaks than the measured results. Especially for the central areas D1b and D2b, there are a series of follow up peaks after the main maximum. Moreover, the shape seems to duplicate two orders of magnitude smaller than the previous one. In D1b, there is only one peak present in the simulation while its measured counterpart presents two. The first and main peak matches the simulation peak in energy and the second one is smaller but maintains the shape of the previous peaks. In D2b, the main peaks in the simulation and the tests seem to match, but after the main first peak, the RADEF histogram presents several other peaks that match the two orders of magnitude smaller description for the second duplicate. This pattern can also be observed in Figures 5 and 6 for other angles.

After identifying some of the main peaks in the simulation/RADEF comparisons, the peaks were matched and manually verified to avoid matching duplicate peaks in the measurements with the peaks of the simulations. The simulations' results were
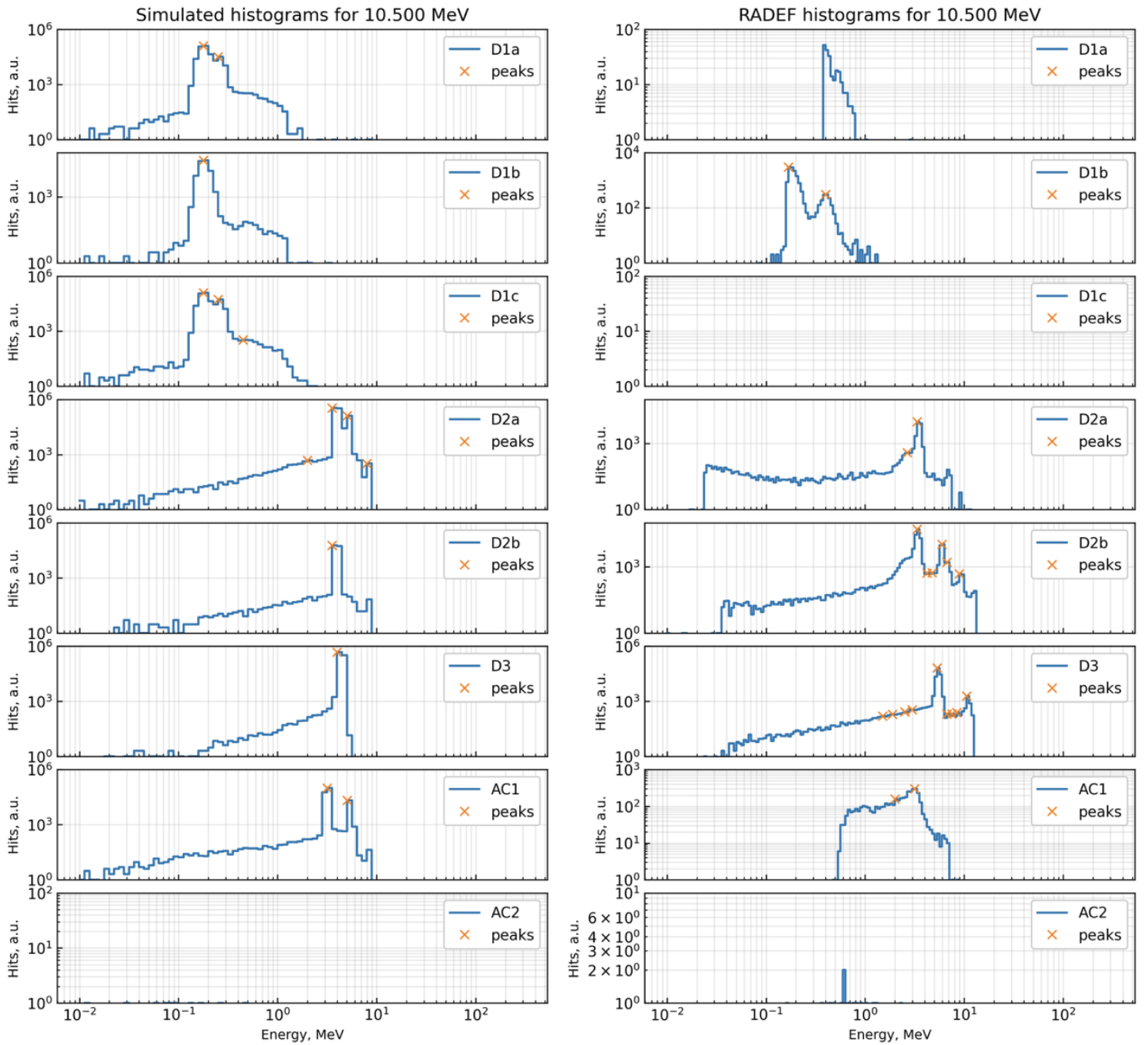
Figure 13.   Histograms for the 10.5 MeV beam with a 200μm aluminium degrader during the simulation with 0° (left) and RADEF test 0°(right).

used as a guide to look for the peaks. The criteria used in this process compared the energy values of the paired histograms and the number of hits counted. If the values agreed, the energy values in the simulation and in the data were correlated. If the values were different, it was assessed if there was a normalising factor between them and no periodic repetition, if so, the energy values were correlated. The discrimination of the artificial peaks had to be evaluated manually to see if the met conditions still gave reasonable matches. The normalising factor condition was especially intricate since it was met several times. However, the periodic repetition condition helped sort the duplicate peaks out. Nevertheless it was checked that the normalising factor was not around two. With these results, a plot of the energy in simulations versus the energy in measurements was carried out. The gain ratios were recalculated with a linear regression of the points available. In some cases only one peak was matched, thus there was only one point in the linear regression. To ensure a complete linear regression the origin was considered as part of the linear regression. This points to a null offset however further assessment would have to be carried out to check the validity of this step. Finally, the gain ratios were calculated with the linear regression slope for each angle for each detection area. The average is presented in Figure 14 with the regression lines.

In Figure 14, we can see the gain ratios for the D1b, D2a, D2b, D3 and AC1 detectors. The gain ratios for D1a, D1c and AC2 are not included. The D1a simulation data usually did not match sufficiently the results from the measurements. The distribution shown in the simulation usually had a slightly different shape than the one observed in the measurement results. The criteria to match the peaks were not homogeneous through the different angles and, as a result, this area was avoided. D1c had a technical problem during the RADEF testing so the trials did not include this detector. Furthermore, AC2 results for the measurements and simulations are consistent. Both, simulations and measurements panels for AC2 show no hits. For
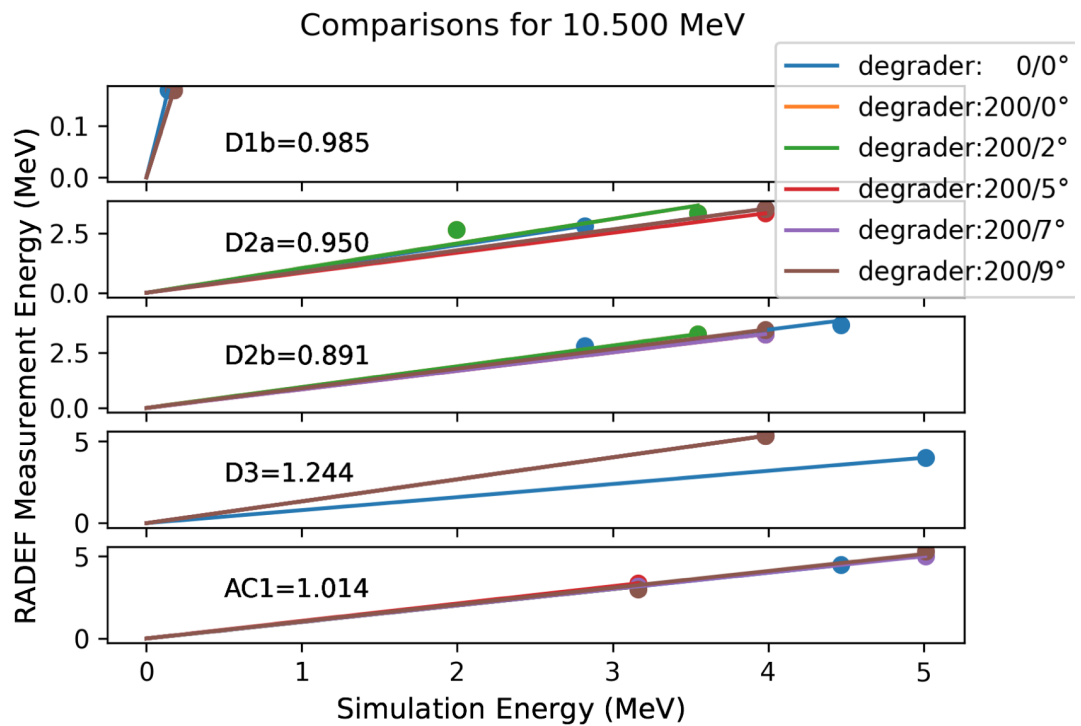
Figure 14.   Simulation energy vs. measurement energy with gain ratios for each detection area. The gain ratios calculated for each of the detectors are generally one for different angles. The final value for each of the gain ratios corresponds to the average value calculated from all the values acquired in the linear regressions for different angles.

D1a = -	**D1b** = 0.984 ± 0.049	**D1c** = -
D2a = 0.949 ± 0.040	**D2b** = 0.891 ± 0.106	
	D3 = 1.243 ± 0.110	
	AC1 = 1.014 ± 0.012	
	AC2 = -	

Table II. Averages of the calculated gain ratios from the linear regression slopes in the first calculation.

zero and nine degrees there are some vertical lines in the measurements panels, and some in the simulation panels for two and five degrees. The scaling in these plots is smaller and can just be showing a background noise detection. Overall, the simulated model fits the observed results for AC2. The gain ratio was calculated to be 1.883. This value does not agree with the expected value of one.

The data set included a comparison for the zero degree measurements with and without the degrader as shown in Figure 15. In the degrader-free histograms, we can appreciate more hits in AC2. The mitigation effect caused by the degrader can also be appraised in the other detectors' energy range. The simulations' and measurements' histograms agree in the results for the hits observed in AC2 with the presence of a degrader.

After carrying out the calculation for all the detectors individually and comparing and assessing the results, a second calculation was made. This second set of linear regressions conserved the origin condition but included all the points for all the angles for each detection area. The linear regression considered all the data points from all the angles in one detector (see Figure 16).

The gain ratios presented in Table II are the average values for all the angles considered and matched. In Table III we have a summary of the gain ratios acquired in the second calculation shown in Figure 16.
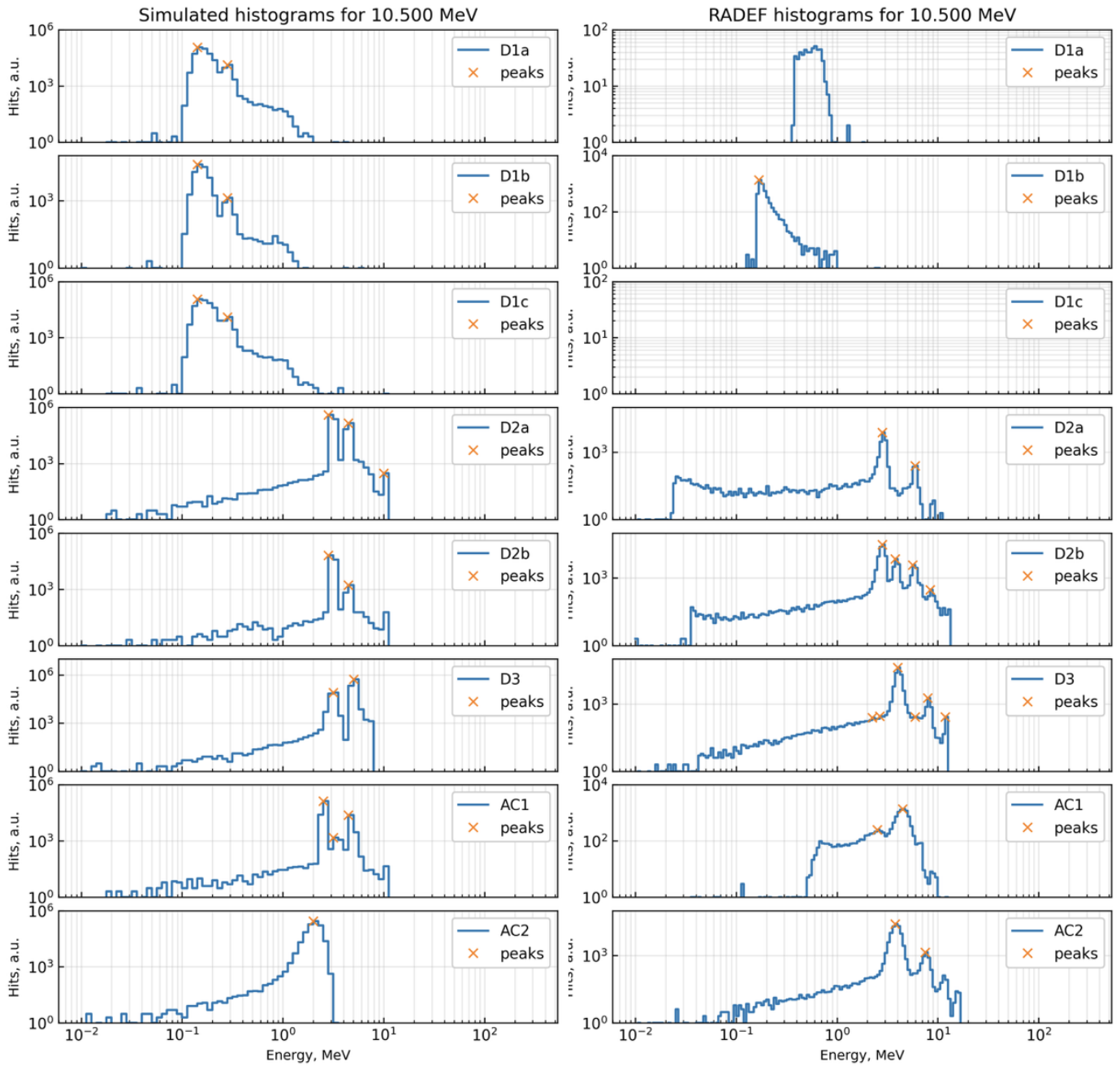
Figure 15. Histograms for the 0° angle with no aluminium degrader during the 10.5 MeV beam simulation (left) and RADEF test (right).
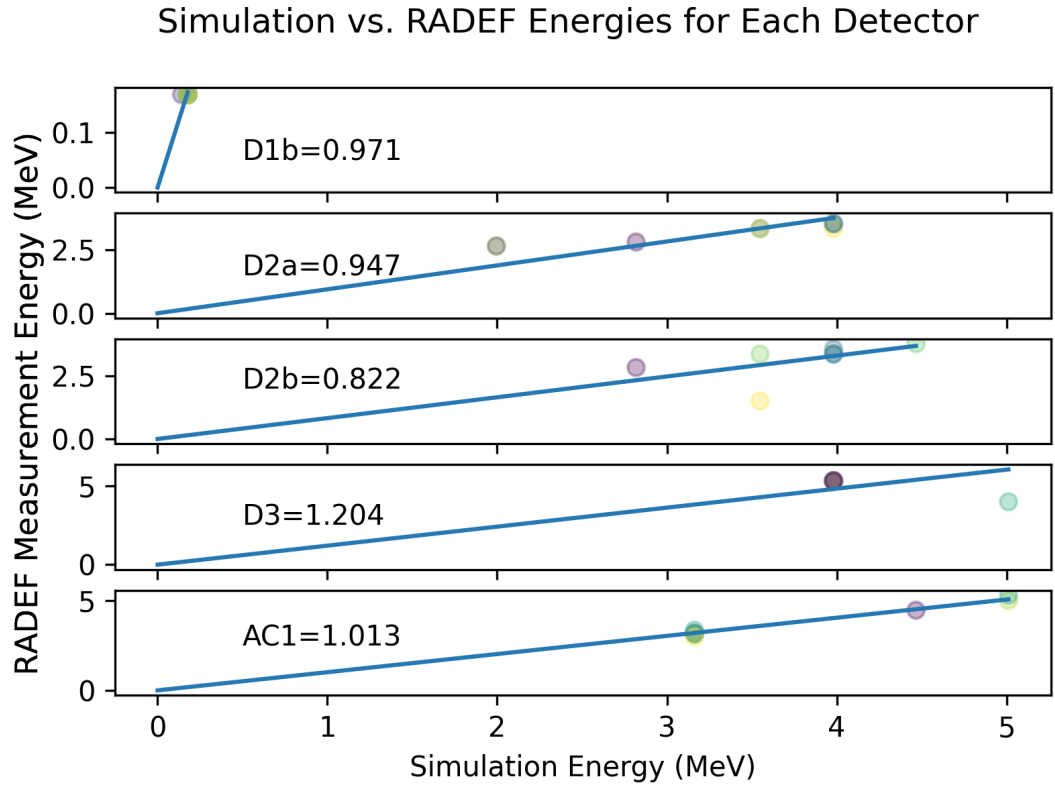
Figure 16.   Simulation energy vs. measurement energy for each detection area. The value for each of the gain ratios corresponds to the slope value of the linear regression considering all the angles in one detector. The points are the correlated peak values in the data and in the simulations.

D1a = -	**D1b** = 0.9714509	**D1c** = -
D2a = 0.94681594	**D2b** = 0.822103	
	D3 = 1.20374495	
	AC1 = 1.01265943	
	AC2 = -	

Table III. Calculated gain ratios from the linear regression slopes considering all the data points from all the angles.

5   Discussion

One of the findings in this work was the duplicate peaks in the histograms of the RADEF measurements. These double peaks are the result of two particles detected too close in time. PATE's electronics pile up the events and create peak replicas of the dual detection treated as single detection. This is shown in the histograms as smaller peaks following the main one. It is easy to identify the main real peaks as the simulation provides a guide for them. The subsequent peaks follow the main peak's shape, and it is around two orders of magnitude smaller than the first peak. Follow-up peaks get smaller but maintain their shape. This deeply affected the gain ratio calculation method as the criteria for matching peaks had to be furthered addressed. Aside from the peaks, no other point was found to be a good candidate to match between the simulation histograms and the histograms of the measurements. The edge was affected by the duplicate peaks and was not a suitable parameter to consider. To construct a linear regression, an extra peak needed to be set. We have selected the origin as a common point between histograms which rules out any offset between simulation and measurements. The trapezoidal filter effectively eliminates any analog offset justifying the choice of the origin as a common point. Moreover, it allows a linear regression slope value equal to the gain ratio for the detection area. Some of the detectors only presented one peak, and thus, the origin completed the information needed for the calculation.

PATE's calibration can be carried out following different methods. The RADEF calibration campaign provided an accelerator facility to test the detector's performance under controlled conditions. Radioactive sources can also be used to calibrate a particle telescope. D1 is the easiest of the stacked-up detectors to calibrate using this technique. An alpha source, Americium 241, is capable of providing alpha particles that D1 can intercept. This radioactive source is a good candidate for the task since alpha particles from Am^{241} are rarely seen in D2. This method would test the

energy response of D1 and the signal path. Different alpha and beta sources can be employed to best fit the properties of each detector. D3 in Figure 14 is presenting a plot were two very different linear regressions are shown. Here, last plotted linear regression is on top of the previous ones that match it. Only the zero degree linear regression does not agree with its partners, and thus only two lines are visible. This detector show the biggest discrepancy with the expected value (one) and the disagreeing line is the main source of error.

The gain ratios calculated partially agree with the expected value of one that would describe a perfect calculation of the gain values. The biggest difference is in D3, while the closest ones are D1b and AC1. The discrepancies in the results can be explained in various ways. The agreement between simulated and measured histograms can improve with the consideration of different angles. The selection of the peaks can be flawed leading to mismatches between the correlated and simulated energies. Moreover, the pairing criteria of the histograms can be insufficient for some cases. Finally, the linear regression can give better results with more data points. Since the gain ratio should not depend on the angle it is possible to employ all the matched points for a detector in the same linear regression. The method was carried out individually, it showed comparative results for each of the detectors with no major flaws in the process. Once the technique was corroborated, another gain ratio calculation was carried out. The results agreed with the previous calculations. More angle data and simulations would offer more correlated data points for the linear regression. However, the individual calculation of the gain ratios allows for an individual appraisal to review if there was an unaccounted for error in a specific angle.

Different factors limited the gain ratio analysis for the detection areas. All the detector areas were studied, but not all of them went through all the analyses. There are no gain ratio calculations for D1a, D1c, or AC2. For D1c, the information could

not be gathered during the RADEF testing because of a technical problem that did not allow the detector to perform. D1a on the other hand, presented problems in the gain ratio calculation process as the results from the measurements had more considerable discrepancies with the simulations than in the rest of the detectors. Since the correlation could not be established, the method did not work for this detector.

The systematic error should also be considered. The angles tested during the RADEF calibration campaign can have some imprecision when setting the angle in the rotating table. The inaccuracy leads to distortions in the histograms and follow-up mismatching with the simulated response. The comparison phase over different angles is a strategic step to minimise this error source. If the measurements' angles are not set precisely, comparing the measurement histograms against a range of different angles can improve the results. It sets the best matches for the measurements against sundry simulated samples. However, the matching decisions taken to pair the simulated response with the measurements data cannot be ruled out as error sources. If the pairing is not carried out optimally the subsequent calculations can present considerable discrepancies from the expected values.

The different methods employed to calculate proxies and analyse the data reveals further details of the device's functioning. It helps understand the observational process and provides information for further studies. The methods employed are usually not the best for all of PATE's components. The analysis and understanding of all the detection elements must be individually assessed and tailored to their specifications. Nevertheless, the different methods provide further information and opportunities to verify results.

6   Conclusions and Outlook

FORESAIL-1/PATE is a developing effort to expand our knowledge and understanding of Earth's space environment. Its findings can help us understand solar processes and their impact on the near-Earth environment. PATE's detection can provide insight into the dynamics of particle populations surrounding Earth and their nature.

The telescope has to undergo a series of tests before being deployed. This is a critical phase since it is the key to understanding how the device functions and determining its performance. The findings will help to prepare further observation and analysis techniques, and detect functionality aspects that need to be taken into account during the space phase of the experiment.

To achieve an understanding of the instrument's performance, different methods have to be employed and combined. Simulations prove to be a powerful tool that let us identify functionality aspects and can also provide an overview of the expected results. The mismatches between simulations and measurements give insights to improve our understanding of the device in space-like conditions. External factors also have to be considered but, in a controlled environment, they can be neglected or easily accounted for. Thus, the results of the simulations and measurements are directly comparable. We analyse them to try to find an explanation for the differences present and see if they agree with the model. This assessment can estimate how suitable the telescope is for the assigned task and how well its ability to function is understood.

Several simulated responses and RADEF measurement results are presented. The mismatches observed gave new information about the detector. Further analysis for the differences in the results points to possible alignment errors during the measurements or flaws in the pairing criteria. The studies of the device in Earth conditions have to be complemented by further trials after deployment. In space,

performance has to be further assessed and studied before starting observations. Further calibration campaigns will take place in flight. These efforts can provide information on the orbital environment and the telescope's role in it. The data gathered can be compared to the simulation response to verify the observations.

References

[1] D. Baker *et al.*, Space Science Reviews **214**, (2017).

[2] J. N. Pelton and F. Allahdadi, in *Handbook of Cosmic Hazards and Planetary Defense*, edited by J. N. Pelton and F. Allahdadi (Springer International Publishing Cham, 2015), pp. 3–33.

[3] P. Krisko, Proceedings of The Institution of Mechanical Engineers Part G-journal of Aerospace Engineering **221**, 975 (2007).

[4] M. Palmroth *et al.*, Journal of Geophysical Research: Space Physics **124**, 5783 (2019).

[5] V. Domingo, in *The Behavior of Systems in the Space Environment*, edited by R. N. DeWitt, D. Duston, and A. K. Hyder (Springer Netherlands Dordrecht, 1993), pp. 67–101.

[6] Y. Kamide and A. C.-L. Chian, *Handbook of the solar-terrestrial environment* (Springer Science & Business Media , 2007).

[7] D. Baker, Advances in Space Research **22**, 7–16 (1998).

[8] S.-I. Akasofu, Journal of Geophysical Research **108**, (2003).

[9] O. E. Malandraki and N. B. Crosby, in *Solar Particle Radiation Storms Forecasting and Analysis: The HESPERIA HORIZON 2020 Project and Beyond*, edited by O. E. Malandraki and N. B. Crosby (Springer International Publishing Cham, 2018), pp. 1–26.

[10] R. Muscheler, in *Encyclopedia of Quaternary Science (Second Edition)*, second edition ed., edited by S. A. Elias and C. J. Mock (Elsevier Amsterdam, 2013), pp. 353–360.

[11] A. Piel, *Plasma Physics* (Springer Berlin Heidelberg , 2010).

[12] G. F. Knoll, *Radiation Detection and Measurement, 3rd ed.*, 3rd edition ed. (John Wiley and Sons New York, 2000).

[13] K. Kleinknecht, *Detectors for particle radiation* (Cambridge Univ. Press Cambridge, United Kingdom, 1986).

[14] *Nuclear Spectroscopy*, Vol. 9 of *Pure and Applied Physics*, edited by F. Ajzenberg-Selove (Elsevier B.V. , 1960), pp. 3–30.

[15] Haug, E., A&A **423**, 793 (2004).

[16] P. Tinyakov, in *Particle Physics Beyond the Standard Model*, Vol. 84 of *Les Houches*, edited by D. Kazakov, S. Lavignac, and J. Dalibard (Elsevier , 2006), pp. 537–572.

[17] R. Blandford and D. Eichler, Physics Reports **154**, 1 (1987).

[18] T. Gombosi *et al.*, Journal of Space Weather and Space Climate (2021).

[19] W. Dröge, in *Energy Conversion and Particle Acceleration in the Solar Corona*, edited by K.-L. Klein (Springer Berlin Heidelberg Berlin, Heidelberg, 2003), pp. 193–212.

[20] F. Singer, Eos Trans. AGU **6**, 329 (1958).

[21] R. Vainio *et al.*, Space Sci Rev **147**, 187 (2009).

[22] Y. Zheng, A. Lui, and M.-C. Fok, Journal of Geophysical Research **115**, (2010).

[23] T. Sarris and X. Li, Annales Geophysicae **23**, 877 (2005).

[24] R. White, Journal of Geophysical Research **72**, (1967).

[25] M. K. Hudson *et al.*, Geophysical Research Letters **22**, 291 (1995).

[26] B. Kress, M. Hudson, and P. Slocum, Geophysical Research Letters **32**, (2005).

[27] J. M. Albert, G. P. Ginet, and M. S. Gussenhoven, Journal of Geophysical Research: Space Physics **103**, 9261 (1998).

[28] R. S. Selesnick, M. D. Looper, and R. A. Mewaldt, Space Weather **5**, (2007).

[29] Y. S. Miyoshi, V. K. Jordanova, A. Morioka, and D. S. Evans, Space Weather **2**, (2004).

[30] A. Vacaresse *et al.*, Journal of Geophysical Research: Space Physics **104**, 28601 (1999).

[31] X. Li and M. Temerin, Space Science Reviews **95**, 569 (2001).

[32] R. Friedel, G. Reeves, and T. Obara, Journal of Atmospheric and Solar-Terrestrial Physics **64**, 265 (2002).

[33] R. Horne and R. Thorne, Geophysical Research Letters **30**, (2003).

[34] J. C. Green and M. G. Kivelson, Journal of Geophysical Research: Space Physics **109**, (2004).

[35] R. H. A. Iles, N. P. Meredith, A. N. Fazakerley, and R. B. Horne, Journal of Geophysical Research: Space Physics **111**, (2006).

[36] R. B. Horne and R. M. Thorne, Geophysical Research Letters **25**, 3011 (1998).

[37] D. Summers, R. M. Thorne, and F. Xiao, Journal of Geophysical Research: Space Physics **103**, 20487 (1998).

[38] R. B. Horne *et al.*, Journal of Geophysical Research: Space Physics **110**, (2005).

[39] C. Chaston *et al.*, Geophysical Research Letters **45**, (2018).

[40] B. Abel and R. M. Thorne, Journal of Geophysical Research: Space Physics **103**, 2397 (1998).

[41] D. Summers and R. M. Thorne, Journal of Geophysical Research: Space Physics **108**, (2003).

[42] J. M. Albert, Journal of Geophysical Research: Space Physics **108**, (2003).

[43] S. Cherry, J. Sorenson, and M. Phelps, *Physics in Nuclear Medicine* (Elsevier B.V., Amsterdam, Netherlands, 2012).

[44] G. F. Knoll, *Radiation Detection and Measurement, 3rd ed.*, 3rd edition ed. (John Wiley and Sons New York, 2000).

[45] M. Krammer, Scholarpedia **10**, 32486 (2015).

[46] B. Wall *et al.*, Nuclear Instruments and Methods in Physics Research Section A: Accelerators, Spectrometers, Detectors and Associated Equipment **744**, 73 (2014).

[47] R. Mewaldt *et al.*, The Astrophysical Journal **693**, L11–L15 (2009).

[48] P. Oleynik *et al.*, Advances in Space Research **66**, (2019).

[49] H. Kettunen *et al.*, in *2014 IEEE Radiation Effects Data Workshop (REDW)* (IEEE , 2014), pp. 1–4.

[50] S. Agostinelli *et al.*, Nuclear Instruments and Methods in Physics Research Section A: Accelerators, Spectrometers, Detectors and Associated Equipment **506**, 250 (2003).

[51] J. Allison *et al.*, IEEE Transactions on Nuclear Science **53**, 270 (2006).

[52] J. Allison *et al.*, Nuclear Instruments and Methods in Physics Research Section A: Accelerators, Spectrometers, Detectors and Associated Equipment **835**, 186 (2016).

7   Appendix A

7.1   Geant4

Geant4 stands for GEometry ANd Tracking. It is a Montecarlo simulation tool used for modelling the paths of particles through matter. This program is usually used in high energy physics, nuclear physics, medical and space sciences, and to study particle colliders. Its content is the result of an international collaboration that maintains and updates it [50], [51], [52]. The code is C++ based and it works with different parts that interlink by defining an inter-phase independently. This develops modules that enable the user to methodically modify even the slightest details of the simulation. This also forces the user to make sure everything is defined before running a simulation, since nothing is predetermined. This can make everything really specific, but also requires vast knowledge of the processes taking place in the simulations. The parameters are incorporated by the C++ code, which makes use of basic abstract classes from the Geant4 scheme. These classes are:

- **G4VUserPhysicsList** A *process* includes all kinds of physical systems such as the photoelectric effect, ionisation or an elastic dispersion whilst a *model* is the description of said process. Every model and process should be orderly placed in the *physics list* of this class to be considered in the simulation.

- **G4VUserDetectorConstruction** The geometry and volumes used in the simulations are defined in this class. Here, the elements, compounds, and mixes from which the detector is made are established and described.

- **G4VUserPrimaryGeneratorAction** In this class, the main characteristics of the simulated particles used as projectiles in the detector are outlined. This covers their positions, momenta, and energies. Geant4 uses the concept of *hits*, which come from the *G4Hit* class. The hits are used to recompile the simulation's data; the information within the *hit* includes energy deposition, momentum, time, and position. The sensitive volumes assigned by *G4VSensitiveDetector*, are processed or saved at the end of each event in a derivative class of *G4VUserEventAction*.

These simulations are usually carried out with *runs*. A *run* is a sequence of *events*; an *event* is the simulation of one or more primary particles and all the subsequent secondary ones. Primary particles are generated by a particle source at a certain position in space at time zero in the beginning of an event. The particles are then moved by *steps* through the simulated geometry. The steps are determined by the physical processes involved. All the created particles are registered and recorded until either their energies are zero, they disappear because of some reaction, or they leave the simulated volume limit (a.k.a. World Volume). If the particles deposit energy in the sensitive volume of the detector, after each step, the simulation will record the information of the deposited energy up to the end of the event. Later, the data can be either analysed or saved permanently.